Available online at www.sciencedirect.com
ScienceDirect
Comput. Methods Appl. Mech. Engrg. 315 (2017) 713–743
Computer methods in applied mechanics and engineering
www.elsevier.com/locate/cma

A *J-integral*-based arc-length solver for brittle and ductile crack propagation in finite deformation-finite strain hyperelastic solids with an application to graphene kirigami

Ettore Barbieri[a,*], Federica Ongaro[a], Nicola Maria Pugno[b,c,a]

[a] *School of Engineering and Materials Science, Queen Mary University of London, Mile End Road, E1 4NS, London, UK*
[b] *Laboratory of Bio-Inspired and Graphene Nanomechanics, Department of Civil, Environmental and Mechanical Engineering, University of Trento, Via Mesiano 77, I-38123 Trento, Italy*
[c] *Centre for Materials and Microsystems, Fondazione Bruno Kessler, Via Sommarive 18, I-38123 Povo (Trento), Italy*

Received 20 July 2016; received in revised form 11 October 2016; accepted 31 October 2016
Available online 10 November 2016

Highlights

- We present a new path-following method for crack propagation in hyperelastic media.
- It provides an explicit formula of the J-integral for different propagation angles.
- It reconciles with the theory of configurational forces and Griffith's balance.
- This arc-length can handle very sharp snap-back paths in the equilibrium curve.
- We present an example to fracture in large strains of graphene kirigami sheets.

Abstract

Arc-length methods based on Newton–Raphson (NR) iterative numerical solvers are indispensable in non-linear mechanics to trace the equilibrium curves of systems with snap-back or snap-through behaviours. An example is a crack propagating in a rubber-like solid, which can generate extremely sharp snap-backs when the elastic energy is released.

A standard arc-length solver satisfies the arc-length constraint which only limits the increment in displacements and in load level to a fixed amount. Thus, it cannot guarantee the satisfaction of the energy balance in the rate form. This work proposes an arc-length based on the J-integral, and assumes the Griffith balance as a constraint equation.

Firstly, a fracture criterion (critical load and direction of crack increment) is formulated, consistent with the thermodynamic principle of maximum dissipation: a crack propagates in the direction of the maximum strain energy release rate. For this purpose, this paper provides an explicit and simple expression of the J-*integral* for varying angles. This fracture criterion does not require the computation of mixed mode Stress Intensity Factors, or asymptotic solutions or derivatives of the tangent stiffness matrix. By doing so, it is shown that the proposed method easily reconciles with the theory of Configurational Forces.

Secondly, because of the explicit expression of J provided in this paper, it is easy to linearize the discretized equations of motions consistently.

The method proves able to handle very sudden snap-backs occurring under large strains, and both brittle and ductile crack propagation. A particular example of such behaviour is *kirigami* (paper-cuts) structures made of graphene. The proposed arc-length can capture, for these structures, the transitions from brittle to ductile crack propagation for the same crack patterns, but different pre-crack lengths.

* Corresponding author.
E-mail address: e.barbieri@qmul.ac.uk (E. Barbieri).

http://dx.doi.org/10.1016/j.cma.2016.10.043

Keywords: Arc-length; Fracture; Hyperelastic; Numerical continuation; Graphene; Kirigami

1. Introduction

The response of a dynamical system (not necessarily mechanical) is given by a set of non-linear first order Ordinary Differential Equations (ODEs). The functional expression of these ODEs might contain several (structural) parameters, and it is often of interest to compute the susceptibility of the static response to such parameters. In static conditions, the initial system of ODEs reduces to a non-linear system of algebraic equations. The roots of this system constitute its *equilibrium curves*, and the techniques to obtain these curves fall under the name of *numerical continuation*. Numerical continuation is a well-established branch of the theory of dynamical systems, and a vast literature exists on this topic. The interested reader can refer to the following cardinal textbooks for an introduction and more detailed references [1–3].

In mechanics, the *equilibrium* is, from a dynamical systems perspective, a single-parameter non-linear problem, with the parameter being a proportional scaling factor of the external forces [4]. The equilibrium curves of a *mechanical* system are, for this reason, often displayed as *force–displacement* diagrams. Equilibrium curves in mechanical systems permit, for example, the computation of the maximum sustainable force, and the detection of critical points of instability and bifurcations. To track the equilibrium curves, one could increase the load level (*load-control*) by small increments; nonetheless, this approach would fail for systems with force–displacement constitutive law. Thus, for these cases, a better option would be to apply displacements, instead of forces, (*displacement-control*): however, this approach would fail for a non-monotonic displacement in the force–displacement constitutive law. These situations are known as *snap-backs* (Fig. 1). Riks [5,6] was the first to propose an *arc-length* method able to trace snap-backs. The idea in the Riks' method is to add a *constraint* equation to the nonlinear system, which would limit both the variations in load level and displacements (Fig. 1). Several variants were proposed to the original algorithm: to name just a few, we mention the line-search [7], local arc-length [8], local arc-length for strain softening [9,10], orthogonal methods [11], asymptotic-numerical methods based on Pade approximants [12–14], dissipation-based arc-length [15–18] and kinetic damping [19].

Recent novel contributions to the field include parallelization [20], gluing of multiple Partial Differential Equations (PDEs) into a single numerical continuation framework [21] and gradient-constrained methods [22]. It is also worth mentioning the availability of free Matlab software [23] for continuation and bifurcation in 2D elliptic systems.

When considering fracture of hyperelastic media in finite deformation, the application of the standard Riks' arc-length would result in overestimating the equilibrium force required to satisfy the Griffith criterion [24]. This will be illustrated with a numerical example in Section 7.3. The reason is that a standard arc-length method only limits the increments in load and displacement, disregarding the energy balance. The dissipation-based arc-length proposed in [15,16] does instead limit the increments in dissipated energy. We discuss the differences between our method and the dissipation-based arc-length more in detail in Section 4.2. For example, [16] applied their method to *geometrically non-linear models* coupled with plasticity and cohesive zone elements. Instead, in this work we propose a framework with non-linearities for both, geometry and material (hyperelasticity), combined with an explicit treatment of strong discontinuities based on a meshfree discretization. Building on the merits of the idea of an *energy-release control* method, we anticipate that a J-integral based approach provides a more direct way to the satisfaction of the Griffith criterion, on the *rate* (in the fracture mechanics' sense) of the energy release.

Moreover, the arc-length proposed in this paper allows simultaneously the incorporation of a criterion for the crack direction. Strictly speaking the non-linear problem becomes a *two-parameters* numerical continuation (the load level λ and the crack orientation θ), as shown in Section 4.3. However, it is shown that it can be transformed into a single-parameter continuation, thanks to an explicit expression of the J*-integral* as a function of θ. This approach allows our method to reconcile with the framework of *configurational forces* for fracture in finite deformation, contained in a series of seminal works [25–30].

To conclude, Section 7 presents several numerical examples. Firstly, the numerical J-integral is validated against an analytical solution of (Section 7.1) from [31–33]; then, the hypothesis behind the fracture criterion is verified by

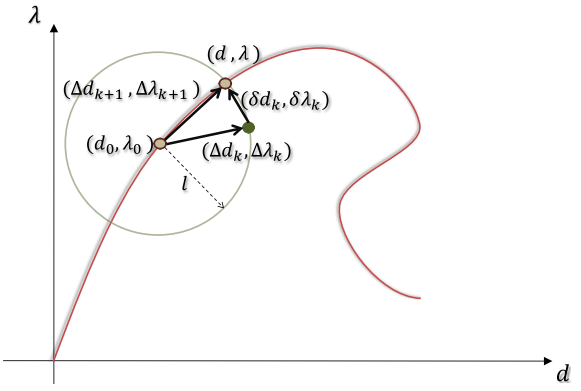

Fig. 1. Spherical arc-length scheme: (d_0, λ_0) is the previously converged state, (d, λ) is the next solution on the path. $(\Delta d_k, \Delta\lambda_k)$ is the increment at the kth iteration. $(\delta d_k, \delta\lambda_k)$ is the iterative step to the increment.

introducing small kinked cracks at the tips of an inclined centred larger crack (Section 7.2); subsequently the proposed method is compared to a standard arc-length, and it is shown its ability to verify the Griffith balance (Section 7.3); next, the propagation of two aligned and misaligned edge-notched cracks (Section 7.4) is studied, with comparisons with the *maximum hoop stress criterion* in the limits of infinitesimal deformations (Section 7.5). Finally, the arc-length is tested for a type of graphene kirigami structure that contains multiple cracks (Section 7.6).

2. Governing equations

2.1. Variational formulation

In this section, the adopted continuum formulation is *Total Lagrangian*, with $\mathcal{B}_0 \subset \mathbb{R}^k$, $k = 2, 3$ being the *reference configuration* at initial time t_0, and $\mathcal{B}_t$ the *deformed configuration* at a generic time t. In the following, $\mathbf{X}$ denote the *material coordinates* and $\mathbf{x}$ the deformation. The deformation is given by the admissible mapping

$$\mathbf{x} = \boldsymbol{\varphi}(\mathbf{X}, t) \qquad \boldsymbol{\varphi} : \left(\mathcal{B}_0 \setminus \Gamma_c^0\right) \times [t_0, t_f] \mapsto \mathcal{B}_t \setminus \Gamma_c \qquad k = 2, 3 \tag{1}$$

with t_f being the final time and Γ_c the image of the current configuration of Γ_c^0. We assume that the mapping is bijective everywhere on $\mathcal{B}_0$ with the exception of Γ_c^0

$$\Gamma_c^0 = \cup_{i=1}^{n_c} \Gamma_{c_i}^0 \qquad \Gamma_{c_i}^0 \subset \mathbb{R}^{k-1} \tag{2}$$

with $\Gamma_{c_i}^0$ being the ith *crack surface* and n_c the number of crack surfaces. It is assumed in the proceeding, that each $\Gamma_{c_i}^0$ can be a *piecewise* set of *segments* for two-dimensional problems, or polygonal flat surfaces for three-dimensional problems. In 2D, for example, for a straight crack,

$$\Gamma_{c_i}^0 = \left\{\mathbf{X} \in \mathcal{B}_0 : \mathbf{X} = \mathbf{X}_{\Gamma_{c_i}^0}\right\} \qquad \mathbf{X}_{\Gamma_{c_i}^0} : [s_0, s_f] \in \mathbb{R} \mapsto \mathbb{R}^{k-1} \qquad \mathbf{X}_{\Gamma_{c_i}^0}(s) = \mathbf{X}_0(1 - s) + \mathbf{X}_1 s \tag{3}$$

with s being the *parameter*, s_0 and s_f being respectively the initial and the final value at time t_0 and t_f, and $\mathbf{X}_0$ and $\mathbf{X}_1$ the *crack-tips*. If $\mathbf{X}_0, \mathbf{X}_1 \in \mathcal{B}_0 \setminus \partial\mathcal{B}_0$, then the crack is *internal*, otherwise, if any of the two tips are on the boundary or outside, the crack is named *edge crack*.

The *deformation gradient* $\mathbf{F}$ is readily obtained as

$$\mathbf{F} = \nabla_0 \boldsymbol{\varphi}(\mathbf{X}, t) \qquad J = \det(\mathbf{F}) > 0 \qquad \mathbf{X} \in \mathcal{B}_0 \setminus \Gamma_c^0 \tag{4}$$

where the subscript $_0$ refers to the material coordinates. We then define the following functionals: the internal energy $\mathcal{W}$

$$\mathcal{W}[\boldsymbol{\varphi}] = \int_{\mathcal{B}_0} w(\mathbf{F}) \mathrm{d}V \tag{5}$$

with w being the *strain energy function* of the hyperelastic constitutive model; the external work functional (in the absence of body forces)

$$\mathcal{P}[\boldsymbol{\varphi}] = \lambda \int_{\Gamma_t^0} \hat{\mathbf{t}}_0^T \mathbf{u}\, \mathrm{d}S + \lambda \int_{\Gamma_u^0} \gamma\, (\mathbf{u} - \bar{\mathbf{u}})^T\, (\mathbf{u} - \bar{\mathbf{u}})\, \mathrm{d}S \tag{6}$$

where $\mathbf{u}$ is the displacement field $\mathbf{u} = \boldsymbol{\varphi}(\mathbf{X}) - \mathbf{X}$, and λ is the load level (the continuation parameter); the boundary $\Gamma_t^0 \subset \partial\mathcal{B}_0$ is where the traction $\lambda\, \hat{\mathbf{t}}_0$ is prescribed, with $\hat{\mathbf{t}}_0$ being a unit vector and λ the load level; $\Gamma_u^0 \subset \partial\mathcal{B}_0$ is the boundary where the displacement $\bar{\mathbf{u}}$ is prescribed, and γ is a penalty factor. Finally, we introduce the *potential energy functional* as

$$\Pi[\boldsymbol{\varphi}] = \mathcal{W}[\boldsymbol{\varphi}] - \mathcal{P}[\boldsymbol{\varphi}]. \tag{7}$$

Fig. 2 show $\mathcal{W}$, $\mathcal{P}$ and Π in a simplified one-dimensional example. The problem is then formulated as: find the motion $\boldsymbol{\varphi}$ or the displacement field $\mathbf{u}$ such that

$$\boldsymbol{\varphi} = \arg \min_{\boldsymbol{\varphi} \in \mathcal{H}^1(\mathcal{B}_0)} \Pi[\boldsymbol{\varphi}] \tag{8}$$

where $\mathcal{H}^1(\mathcal{B}_0)$ is the space of vectorial functions in $\mathcal{L}^2(\mathcal{B}_0)$ that are *square-integrable* along with their first derivatives. Since we are interested in equilibrium conditions, the kinetic energy functional is not considered here. However, for the sake of an iterative numerical scheme, it is appropriate to define the rate quantities and the variations of the functionals in Eqs. (5)–(7).

$$\dot{\mathcal{W}}[\dot{\boldsymbol{\varphi}}, \boldsymbol{\varphi}] = \int_{\mathcal{B}_0} \dot{w}(\mathbf{F})\mathrm{d}V = \int_{\mathcal{B}_0} \frac{\partial w}{\partial \mathbf{C}} : \dot{\mathbf{C}}\, \mathrm{d}V = \int_{\mathcal{B}_0} \frac{1}{2}\mathbf{S} : 2\dot{\mathbf{E}}\, \mathrm{d}V = \int_{\mathcal{B}_0} \mathbf{S} : \dot{\mathbf{E}}\, \mathrm{d}V \tag{9}$$

where $\mathbf{C}$ is the *Right Cauchy–Green* tensor, $\mathbf{E}$ is the *Green–Lagrange* strain tensor, $\mathbf{S}$ is the *Second Piola–Kirchhoff* stress tensor

$$\mathbf{C} = \mathbf{F}^T\mathbf{F} \qquad \mathbf{E} = \frac{1}{2}(\mathbf{C} - \mathbf{I}) \qquad \mathbf{S} = 2\frac{\partial w}{\partial \mathbf{C}} \tag{10}$$

and the corresponding variation is

$$\delta\mathcal{W}[\delta\boldsymbol{\varphi}, \boldsymbol{\varphi}] = \int_{\mathcal{B}_0} \mathbf{S} : \delta\mathbf{E}\, \mathrm{d}V. \tag{11}$$

The rate of the external work is

$$\dot{\mathcal{P}}[\dot{\boldsymbol{\varphi}}, \boldsymbol{\varphi}] = \lambda \int_{\Gamma_t^0} \hat{\mathbf{t}}_0^T \dot{\mathbf{u}}\, \mathrm{d}S + \lambda \int_{\Gamma_u^0} \gamma \dot{\mathbf{u}}^T\, (\mathbf{u} - \bar{\mathbf{u}})\, \mathrm{d}S \tag{12}$$

with the corresponding variation

$$\delta\mathcal{P}[\delta\boldsymbol{\varphi}, \boldsymbol{\varphi}] = \lambda \int_{\Gamma_t^0} \hat{\mathbf{t}}_0^T\, \delta\mathbf{u}\, \mathrm{d}S + \lambda \int_{\Gamma_u^0} \gamma\, \delta\mathbf{u}^T\, (\mathbf{u} - \bar{\mathbf{u}})\, \mathrm{d}S. \tag{13}$$

Eq. (8) can be reformulated as

$$\delta\Pi[\delta\boldsymbol{\varphi}, \boldsymbol{\varphi}] = \delta\Pi[\delta\mathbf{u}, \mathbf{u}] = 0 \tag{14}$$

that is

$$\int_{\mathcal{B}_0} \delta\mathbf{E} : \mathbf{S}\mathrm{d}V - \int_{\Gamma_t^0} \delta\mathbf{u}^T\, \lambda\hat{\mathbf{t}}_0\, \mathrm{d}S\, - \gamma \int_{\Gamma_u^0} \delta\mathbf{u}^T\, (\mathbf{u} - \bar{\mathbf{u}})\, \mathrm{d}S = 0. \tag{15}$$

Another rate of interest is the *strain energy release rate* G.

$$G\left[\boldsymbol{\varphi}_a\right] = -\frac{\partial \Pi\left[\boldsymbol{\varphi}_a\right]}{\partial A} = \frac{\partial \mathcal{P}\left[\boldsymbol{\varphi}_a\right]}{\partial A} - \frac{\partial \mathcal{W}\left[\boldsymbol{\varphi}_a\right]}{\partial A} = \frac{1}{2B} \lim_{\Delta a \to 0} -\frac{\Pi\left[\boldsymbol{\varphi}_{a+\Delta a}\right] - \Pi\left[\boldsymbol{\varphi}_a\right]}{\Delta a} \tag{16}$$

where $A = 2\ B\ a$ is the crack surface area, where B is the thickness of the body (in 2D), and a is the crack length.

$$a = \int_{\Gamma_c^0} \mathrm{d}s. \tag{17}$$

The subscript $_a$ in Eq. (16) indicates the motion of the body $\mathcal{B}_0$ containing cracks Γ_c^0 of measure a. The term *rate* is intended in the *fracture mechanics'* sense, meaning *with respect to the fracture area*, and not *with respect to time*.

2.2. Discretized equations of motion

Because of the ease of introducing discrete cracks without remeshing, we will use a meshfree setting, namely the Reproducing Kernel Particle Method (RKPM) [34]. For the explicit treatment of cracks, we follow the *intrinsic enrichment* presented in [35–37].

Let us first define the functional spaces for the test and the trial functions. We adopt a Bubnov–Galerkin method, for which test $\delta\mathbf{u}(\mathbf{X})$ and trial $\mathbf{u}(\mathbf{X})$ vectorial functions are chosen in affine spaces. For the test functions, we select the following Sobolev space $\mathcal{V}$ defined as:

$$\delta\mathbf{u}(\mathbf{X}) \in \mathcal{V} \quad \mathcal{V} = \left\{ \delta\mathbf{u}(\mathbf{X}) \in \mathcal{H}^1(\mathcal{B}_0) \mid \delta\mathbf{u}(\mathbf{X}) = \mathbf{0} \in \Gamma_u \right\} \tag{18}$$

whilst for the trial functions, we select the Sobolev space $\mathcal{S}$

$$\mathbf{u}(\mathbf{X}) \in \mathcal{S} \qquad \mathcal{S} = \left\{ \mathbf{u}(\mathbf{X}) \in \mathcal{H}^1(\mathcal{B}_0) \right\}. \tag{19}$$

In the definition (19) we purposely left out the constraints imposed by the essential boundary conditions since the RKPM approximation used in the weak form does not satisfy the Kronecker condition. Therefore, essential boundary conditions will be enforced through penalty conditions. Furthermore, we pose no restrictions on the continuity of these functions, since we are seeking a discontinuous approximation.

2.3. RKPM approximation

We discretize the body $\mathcal{B}_0$ with a cover of N overlapping spheres $\mathcal{Q}_I \subset \mathcal{B}_0$ of variable radii $r_I,\ I = 1, \ldots, N_i$, such that $\mathcal{B}_0 \subset \bigcup_{I=1}^{N} \mathcal{Q}_I$. We call *nodes* the centres of these spheres $\mathbf{X}_I$, and we consider h as an average measure of the distance between two neighbouring nodes. Because of the overlap, $h < r_I,\ I = 1, \ldots, N$.

We can then define the finite dimensional subspaces $\mathcal{V}^h \subset \mathcal{V}$ and $\mathcal{S}^h \subset \mathcal{S}$ of approximating functions

$$\mathcal{S}^h = \left\{ \mathbf{u}^h \in \mathcal{H}^1(\mathcal{B}_0) \mid \mathbf{u}^h \in \mathcal{R}^1(\mathcal{B}_0) \right\} \tag{20}$$

where $\mathcal{R}^1$ is the functional space of the RKPM functions, with *reproducibility* up to the first order. Conversely to finite element functional spaces, functions in $\mathcal{R}^1$ are defined globally over the body $\mathcal{B}_0$: the local character is maintained because the shape functions are *compact support* functions, that is they are null beyond the radius r_I. Furthermore, functions in $\mathcal{R}^1$ remain in this space even if they are discontinuous.

The functions $\mathbf{u}^h \in \mathcal{S}^h$ (and similarly $\delta\mathbf{u}^h \in \mathcal{V}^h$) are expressed as a linear combination

$$\mathbf{u}^h(\mathbf{X}, t) = \sum_{I=1}^{N_i} \phi_I(\mathbf{X})\ \mathbf{d}_I(t) \tag{21}$$

$$\delta\mathbf{u}_h^T(\mathbf{X}) = \sum_{I=1}^{N_i} \delta\mathbf{d}_I^T\ \phi_I^T(\mathbf{X}) \tag{22}$$

where $\mathbf{d}_I(t)$ are *nodal coefficients* (not nodal values) and $\phi_I(\mathbf{X})$ *shape functions* centred in $\mathbf{X}_I$

$$\mathbf{d}_I^T = \begin{bmatrix} U_I^T & V_I^T & W_I^T \end{bmatrix}. \tag{23}$$

The shape functions are computed as

$$\phi_I(\mathbf{X}) = \omega(\mathbf{X}_I, \mathbf{X})\mathbf{P}(\mathbf{X})^T \mathsf{M}^{-1}(\mathbf{X})\mathbf{P}(\mathbf{X}_I) \tag{24}$$

where the weighting function is defined as

$$\omega(\mathbf{X}_I, \mathbf{X}) = \Delta V_I\, w\left(\frac{|\mathbf{X}_I - \mathbf{X}|}{r_I}\right) \tag{25}$$

with ΔV_I a measure of the sphere of radius r_I centred in $\mathbf{X}_I$, $\mathbf{P}(\mathbf{X})$ denotes a complete basis of the subspace of polynomials of degree k, $\mathbf{P}(\mathbf{X}) = \{p_0(\mathbf{X}), p_1(\mathbf{X}), \ldots, p_k(\mathbf{X})\}$, and M is the *moment matrix*

$$\mathsf{M}(\mathbf{X}) = \sum_{I \in \mathcal{S}_{\mathbf{X}}{}^r} \omega(\mathbf{X}_I, \mathbf{X})\mathbf{P}(\mathbf{X}_I)\mathbf{P}(\mathbf{X}_I)^T \tag{26}$$

where the index set $\mathcal{S}_{\mathbf{X}}{}^r$

$$\mathcal{S}_{\mathbf{X}}{}^r = \left\{J \in \{1, 2, \ldots, N\} \quad | \quad \|\mathbf{X} - \mathbf{X}_J\| \leq r_J\right\}. \tag{27}$$

The moment matrix M can also be viewed as a Gram matrix defined with a discrete scalar product

$$\langle u, v\rangle_{\mathbf{X}} = \sum_{I \in \mathcal{S}_{\mathbf{X}}{}^r} \omega(\mathbf{X}_I, \mathbf{X})u(\mathbf{X}_I)v(\mathbf{X}_I) \tag{28}$$

and, from a numerical point of view, it is convenient to work with a centred and scaled version to enhance the condition number of the system of normal equations. This correction implies that the following definition of M is adopted here

$$\mathsf{M}(\mathbf{X}) = \sum_{I \in \mathcal{S}_{\mathbf{X}}{}^r} \omega(\mathbf{X}_I, \mathbf{X})\mathbf{P}\left(\frac{\mathbf{X}_I - \mathbf{X}}{r}\right)\mathbf{P}^T\left(\frac{\mathbf{X}_I - \mathbf{X}}{r}\right) \tag{29}$$

where r denotes the average of all the compact support radii. The matrix M can be inverted quickly using an iterative algorithm based on the Sherman–Morrison formula [38] which provides explicit equations for M^{-1} and proved to reduce sensibly the computational costs associated with Eqs. (29) and (24).

The continuity properties of the RKPM shape functions are clearly linked to the continuity properties of the function w in Eq. (25), which is usually referred to as the *kernel* of the approximation. This work considers the so-called *2kth order spline*, which is the C^{k-1} function given by

$$w(\xi) = \begin{cases} (1-\xi^2)^k & 0 \leq \xi \leq 1 \\ 0 & \xi > 1. \end{cases} \tag{30}$$

The *reproducibility* is given by using as nodal coefficients the polynomial basis $\mathbf{P}$ computed in the nodes $\mathbf{x}_I$:

$$\begin{aligned} \mathbf{u}^h(\mathbf{X}) &= \sum_{I=1}^{N_i} \phi_I(\mathbf{X})\mathbf{P}(\mathbf{X}_I)^T = \mathbf{P}(\mathbf{X})^T \mathsf{M}^{-1}(\mathbf{X}) \sum_{I=1}^{N_i} \omega(\mathbf{X}_I, \mathbf{X})\mathbf{P}(\mathbf{X}_I)\mathbf{P}(\mathbf{X}_I)^T \\ &= \mathbf{P}(\mathbf{X})^T \mathsf{M}^{-1}(\mathbf{X})\mathsf{M}(\mathbf{X}) = \mathbf{P}(\mathbf{X})^T \end{aligned} \tag{31}$$

meaning that the approximation $\mathbf{u}_h(\mathbf{X})$ is *interpolative* to all the functions in the basis $\mathbf{P}$. To impose the discontinuity introduced by the presence of a crack, we use an *intrinsic enrichment*, where the RKPM shape functions (24) are rendered simultaneously discontinuous over the crack segments, and continuous around the crack tips. For a more complete description, the reader is invited to refer to [35,36,39] for curved cracks described by Non-Uniform Rational B-Spline (NURBS) parametrizations.

2.4. Discrete balance equations

Following [40], using Eq. (21), the discretized variation of the deformation gradient becomes

$$\delta\mathbf{F}^h = \delta\mathbf{d}\, \mathbb{B}_0^T \tag{32}$$

with

$$\mathbb{B}_0^T = \begin{bmatrix} \dfrac{\partial \boldsymbol{\phi}^T}{\partial X_1} & \dfrac{\partial \boldsymbol{\phi}^T}{\partial X_2} \end{bmatrix} \tag{33}$$

and the following holds

$$\delta \mathbf{F} : \mathbf{P} = \delta \mathbf{E} : \mathbf{S}. \tag{34}$$

Replacing (21) into (15), the following equilibrium equations are obtained

$$\mathbf{F}^{(i)}(\mathbf{d}) - \lambda \mathbf{F}^{(e)} = 0 \tag{35}$$

where λ is the load level, $\mathbf{F}^{(e)}$ is the *external forces* vector

$$\mathbf{F}^{(e)} = \int_{\Gamma_u} \begin{bmatrix} \boldsymbol{\phi}^T & 0 \\ 0 & \boldsymbol{\phi}^T \end{bmatrix} \hat{\mathbf{t}}_0 \mathrm{d}\Gamma_u. \tag{36}$$

$\mathbf{F}^{(i)}$ is the *internal forces* vector that depends on the *constitutive model* of the material

$$\delta \mathbf{d}^T \mathbf{F}^{(i)}(\mathbf{d}) = \int_{\mathcal{B}_0} \delta \mathbf{E}^h : \mathbf{S}^h \, \mathrm{d}V = \int_{\mathcal{B}_0} \delta \mathbf{F}^h : \mathbf{P}^h \, \mathrm{d}V = \delta \mathbf{d}^T \int_{\mathcal{B}_0} \begin{bmatrix} \dfrac{\partial \boldsymbol{\phi}}{\partial X_1} P_{11}^h(\mathbf{d}) + \dfrac{\partial \boldsymbol{\phi}}{\partial X_2} P_{21}^h(\mathbf{d}) \\ \dfrac{\partial \boldsymbol{\phi}}{\partial X_1} P_{12}^h(\mathbf{d}) + \dfrac{\partial \boldsymbol{\phi}}{\partial X_2} P_{22}^h(\mathbf{d}) \end{bmatrix} \mathrm{d}V \tag{37}$$

hence

$$\mathbf{F}^{(i)} = \int_{\mathcal{B}_0} \begin{bmatrix} \dfrac{\partial \boldsymbol{\phi}}{\partial X_1} P_{11}^h(\mathbf{d}) + \dfrac{\partial \boldsymbol{\phi}}{\partial X_2} P_{21}^h(\mathbf{d}) \\ \dfrac{\partial \boldsymbol{\phi}}{\partial X_1} P_{12}^h(\mathbf{d}) + \dfrac{\partial \boldsymbol{\phi}}{\partial X_2} P_{22}^h(\mathbf{d}) \end{bmatrix} \mathrm{d}V. \tag{38}$$

2.5. Tangent stiffness matrix

For each iteration, it is necessary to compute the *tangent stiffness matrix* $\mathbf{K}_T$ of the internal forces. It can be shown that

$$\mathbf{K}_T = \frac{\partial \mathbf{F}^{(i)}}{\partial \mathbf{d}} = \mathbf{K}_T^g + \mathbf{K}_T^m \tag{39}$$

where superscript $(\cdot)^g$ stands for *geometric part*, which takes into account geometrical nonlinearities

$$\mathbf{K}_T^g = \int_{\mathcal{B}_0} \begin{bmatrix} \mathbb{B}_0^T \mathbf{S}^h(\mathbf{u}^h) \mathbb{B}_0 & \\ & \mathbb{B}_0^T \mathbf{S}^h(\mathbf{u}^h) \mathbb{B}_0 \end{bmatrix} \mathrm{d}V \tag{40}$$

where $\mathbf{S}$ is in Voigt notation. Instead, $(\cdot)^m$ stands for the *material part*, which takes into account material nonlinearities

$$\mathbf{K}_T^m = \int_{\Omega_0} \mathbf{B}^{h\,T}(\mathbf{u}^h) \, \mathbf{A}^{\mathrm{SE}}(\mathbf{u}^h) \, \mathbf{B}^h(\mathbf{u}^h) \, \mathrm{d}V \tag{41}$$

where

$$\mathbf{B}^h(\mathbf{d}) = \begin{bmatrix} F_{11}^h \dfrac{\partial \boldsymbol{\phi}}{\partial X_1}^T & F_{21}^h \dfrac{\partial \boldsymbol{\phi}}{\partial X_1}^T \\ F_{12}^h \dfrac{\partial \boldsymbol{\phi}}{\partial X_2}^T & F_{22}^h \dfrac{\partial \boldsymbol{\phi}}{\partial X_2}^T \\ F_{11}^h \dfrac{\partial \boldsymbol{\phi}}{\partial X_2}^T + F_{12}^h \dfrac{\partial \boldsymbol{\phi}}{\partial X_1}^T & F_{21}^h \dfrac{\partial \boldsymbol{\phi}}{\partial X_2}^T + F_{22}^h \dfrac{\partial \boldsymbol{\phi}}{\partial X_1}^T \end{bmatrix} \tag{42}$$

and $\mathbf{A}^{\mathrm{SE}}$ is the *Second Elasticity Tensor* in Voigt form, defined, in tensorial form, as

$$\mathcal{A}^{(2)} = \frac{\partial \mathbf{S}}{\partial \mathbf{E}}. \tag{43}$$

2.6. The constitutive model

In all the following examples, we will assume *plane stress* and *incompressible* Neo-Hookean material. In this case, the *pressure* p can be explicitly determined. Indeed, following [41], the strain energy *density* function w is

$$w(\mathbf{C}) = \frac{1}{2}\mu_0 \left(I_1 - 3\right) \tag{44}$$

where μ_0 is the *initial* shear modulus, I_1 is the first invariant of the Right Cauchy–Green tensor.

The corresponding Second Piola–Kirchhoff Stress is

$$\mathbf{S} = \mu_0 \mathbf{I} - p\mathbf{C}^{-1}. \tag{45}$$

The pressure is given by

$$p = \frac{1}{\det\left(\bar{\mathbf{C}}\right)} \bar{\mathbf{C}}^{-1} \tag{46}$$

where the bar indicates the 2×2 in-plane components of the tensor.

The second elasticity tensor is

$$\mathcal{A}^{(2)} = 2\mu \frac{1}{\det\left(\bar{\mathbf{C}}\right)} \left(\bar{\mathbf{C}}^{-1} \otimes \bar{\mathbf{C}}^{-1} + \mathcal{I}\right) \tag{47}$$

where

$$\mathcal{I} = \frac{\partial \bar{\mathbf{C}}^{-1}}{\partial \bar{\mathbf{C}}^{-1}}. \tag{48}$$

3. Crack propagation criterion

The Griffith criterion [24] states that for a crack of initial length a to grow, the following condition needs to verify

$$G\left[\boldsymbol{\varphi}_a\right] - G_c(a) = 0 \tag{49}$$

where G_c is the *critical strain energy release rate* of the material, and G is defined in Eq. (16). For brittle fracture, G_c is independent of the crack length a, for ductile fracture instead, $G_c = G_c(a)$. The functional $\mathcal{P}$ (in Eq. (6)) for a discretized medium, becomes, for *deformation-independent* loads

$$\mathcal{P}\left[\boldsymbol{\varphi}_a^h\right] = \lambda \mathbf{F}^{(e)\,T}\mathbf{d} = \mathbf{F}^{(i)\,T}\mathbf{d} \tag{50}$$

where the last step used Eq. (35).

The rate of the internal energy, in Eq. (9), becomes

$$\dot{\mathcal{W}}\left[\dot{\boldsymbol{\varphi}}_a^h, \boldsymbol{\varphi}_a^h\right] = \mathbf{F}^{(i)\,T}\dot{\mathbf{d}}. \tag{51}$$

For large displacements and small strains, there is a linear relation between the Green–Lagrange Strain $\mathbf{E}$ and the *Second Piola–Kirchhoff* stress $\mathbf{S}$. Therefore, $\mathcal{W}$ can be simply written as

$$\mathcal{W}\left[\boldsymbol{\varphi}_a^h\right] = \frac{1}{2}\int_{\Omega_0} \mathbf{S} : \mathbf{E}\, \mathrm{d}V = \frac{1}{2}\mathbf{F}^{(i)\,T}\,\mathbf{d} = \frac{1}{2}\,P. \tag{52}$$

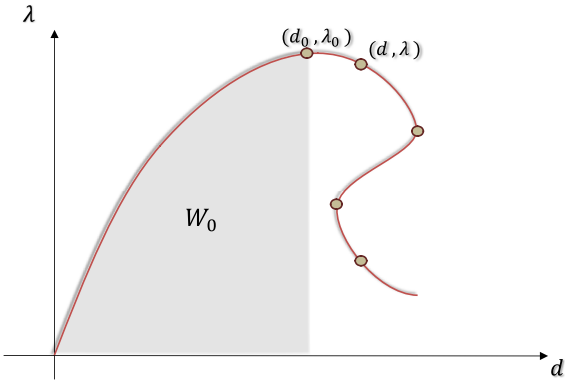

(a) Strain energy at crack length a.

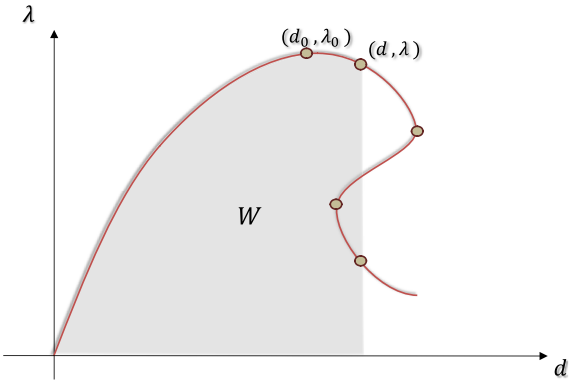

(b) Strain energy at crack length $a + \Delta a$.

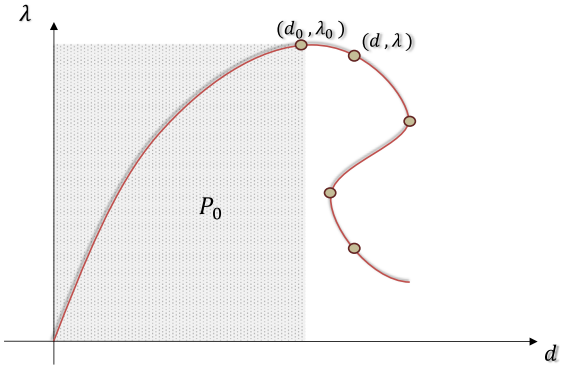

(c) External work at crack length a.

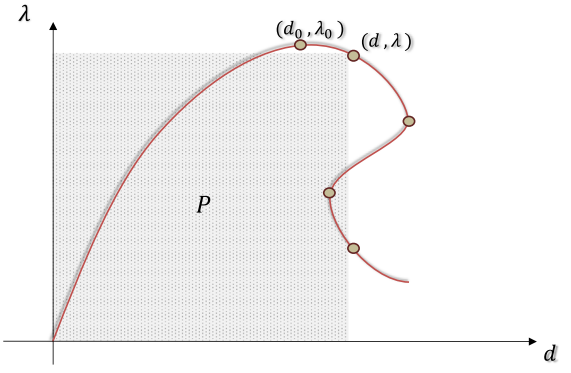

(d) External work at crack length $a + \Delta a$.

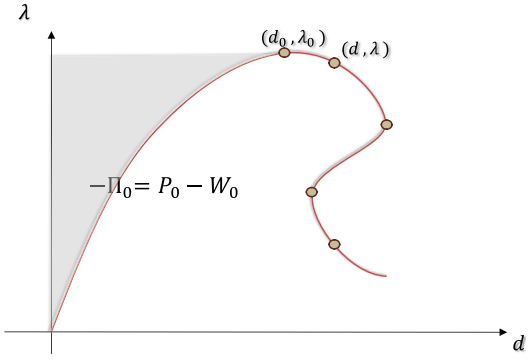

(e) Potential energy at crack length a.

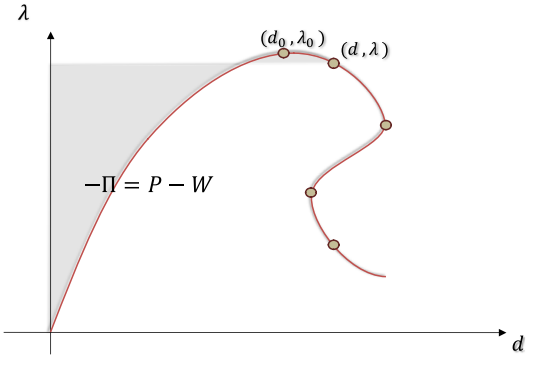

(f) Potential energy at crack length $a + \Delta a$.

Fig. 2. Definition of strain energy release rate between two equilibrium states: $G = -\frac{\partial \Pi}{\partial A}$, with A being the crack surface area.

For geometrically non-linear constitutive material models, with both displacements and strains being large, Eq. (52) is not valid. Integrating by parts Eq. (51)

$$\mathcal{W}\left[\boldsymbol{\varphi}_a^h\right] = \int_0^{\mathbf{d}} \mathbf{F}^{(i)\,T}\,\mathrm{d}\,\mathbf{d} = \mathbf{F}^{(i)\,T}\mathbf{d} - \int_0^{\mathbf{d}} \left(\frac{\partial \mathbf{F}^{(i)\,T}}{\partial \mathbf{d}}\,\mathbf{d}\right)^T \mathrm{d}\,\mathbf{d} = P - \int_0^{\mathbf{d}} \mathbf{d}^T\,\mathbf{K}_T\,\mathrm{d}\,\mathbf{d} = \int_0^{\mathbf{d}} \mathbf{d}^T\,\mathrm{d}\mathbf{F}^{(i)} \tag{53}$$

where in the last step we used the definition of *tangent stiffness matrix*. Therefore,

$$-\Pi\left[\boldsymbol{\varphi}_a^h\right] = \mathcal{P}\left[\boldsymbol{\varphi}_a^h\right] - \mathcal{W}\left[\boldsymbol{\varphi}_a^h\right] = \int_0^{\mathbf{d}} \mathbf{d}^T\,\mathrm{d}\mathbf{F}^{(i)} = \int_0^{\mathbf{d}} \mathrm{d}\mathbf{F}^{(i)\,T}\mathbf{d} \tag{54}$$

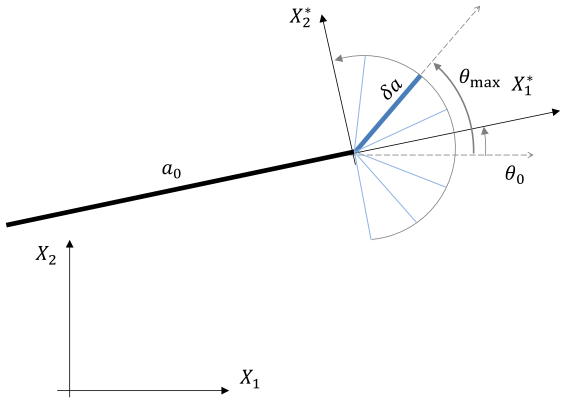

Fig. 3. Fracture criterion: a crack of length a_0 (black thick line) with initial inclination θ_0 propagates as an infinitesimal virtual kink (blue thick line) $\delta a \ll a_0$ in the direction $\theta_{\max}$ of *maximum energy release rate*. (For interpretation of the references to colour in this figure legend, the reader is referred to the web version of this article.)

which, for the Griffith criterion,

$$G\left[\boldsymbol{\varphi}_a^h\right] = -\frac{\partial \Pi\left[\boldsymbol{\varphi}_a^h\right]}{\partial A} = \frac{\partial}{\partial A}\int_0^{\mathbf{d}} \mathrm{d}\mathbf{F}^{(i)\,T}\mathbf{d} = G_c(a). \tag{55}$$

Fig. 3 depicts the proposed fracture criterion. The initial crack of length a_0 will propagate in the direction $\theta_{\max}$ of *maximum strain energy release rate* G. This criterion is commonly adopted in fracture mechanics [26,27]. The assumption in this paper is that the G at crack $a_0 + \delta a$ is computed *before* the crack is actually introduced, that is, at crack length a_0. In fact, we hypothesize that the initial crack grows with an infinitesimal *virtual* kink δa, much smaller than the original length. In this case, the stress states at a_0 and $a_0 + \delta a$ are not substantially different. Therefore, G at $a_0 + \delta a$ can be computed by rotating of an angle θ the relevant quantities (stress and displacement gradients) at a_0. This variation of the J-integral with the angle has an explicit expression, as explained in the proceeding of the section. This means that J at any angle θ can be computed from the fields in the original frame $\mathbf{X} = [X_1, X_2]$ (see Fig. 3). This explicit expression turns out to be a simple trigonometric function, easy to maximize. The hypothesis behind the criterion is verified in an example in Section 7.2.

The J-integral for finite deformation can be written as

$$J\left[\boldsymbol{\varphi}_a\right] = [1\ 0]\int_{\mathcal{D}_\rho}\left(\nabla_0^* \mathbf{u}^{*T}\mathbf{P}^* - w\mathbf{I}\right)\nabla_0^* q\,\mathrm{d}S \tag{56}$$

where the domain $\mathcal{D}_\rho$ is a circle around the crack-tip of radius ρ, $\mathbf{P}$ is the *First Piola–Kirchhoff* stress, w is the *strain energy density* function and q is a *weight function*

$$q : \mathcal{D}_\rho \subset \mathcal{B}_0 \mapsto [0,1] \qquad q(\mathbf{X}) = \begin{cases} 0 & \mathbf{X} \in \partial\mathcal{D}_\rho \\ 1 & \mathbf{X} \text{ is a crack-tip.} \end{cases} \tag{57}$$

The tensors in Eq. (56) need to be rotated in the local reference frame, indicated by the superscript *. The quantities in Eq. (56) transform according to the following laws:

$$\nabla_0^* \mathbf{u}^* = \mathbf{R}(\theta)^T\ \nabla_0 \mathbf{u}\ \mathbf{R}(\theta) \tag{58}$$

because the displacement gradient transforms as a second-order tensor, with rotation tensor $\mathbf{R}$

$$\mathbf{R}(\theta) = \begin{bmatrix} \cos(\theta) & -\sin(\theta) \\ \sin(\theta) & \cos(\theta) \end{bmatrix} \tag{59}$$

$$\nabla_0^* q = \mathbf{R}(\theta)^T \nabla_0 q. \tag{60}$$

The First Piola–Kirchhoff, instead, transforms as a vector

$$\mathbf{P}^* = \mathbf{R}(\theta)^T \mathbf{P}. \tag{61}$$

On the basis of an infinitesimal crack kink, the J-integral at a propagating crack tip can be expressed in a rotated coordinate system as

$$J\left[\boldsymbol{\varphi}_a^h\right] = J(\mathbf{d},\theta) = [1\ 0]\int_{\mathcal{D}_\rho}\left[\left(\mathbf{R}(\theta)^T\ \nabla_0\mathbf{u}^h\ \mathbf{R}(\theta)\right)^T\left(\mathbf{R}(\theta)^T\mathbf{P}^h\right) - w^h\mathbf{I}\right]\mathbf{R}(\theta)^T\nabla_0 q\ \mathrm{d}S \tag{62}$$

that can be rearranged as

$$J(\mathbf{d},\theta) = [1\ 0]\int_{\mathcal{D}_\rho}\mathbf{R}(\theta)^T\left(\nabla_0\mathbf{u}^{hT}\mathbf{P}^h - w^h\mathbf{I}\right)\mathbf{R}(\theta)^T\nabla_0 q\mathrm{d}S \tag{63}$$

where the term in the round brackets depends on $\mathbf{d}$.

Expanding Eq. (63), it is possible to obtain

$$J(\mathbf{d},\theta) = J_1(\mathbf{d})\cos(\theta) + J_2(\mathbf{d})\sin(\theta) = \mathbf{j}^h(\mathbf{d})\cdot\mathbf{e} \tag{64}$$

where $\mathbf{e} = \mathbf{e}(\theta) = [\cos(\theta), \sin(\theta)]$ is the unit vector of the direction of propagation of the crack, and $\mathbf{j}^h = \mathbf{j}^h(\mathbf{d}) = [J_1(\mathbf{d}), J_2(\mathbf{d})]$.

$$J_1(\mathbf{d}) = \int_S \frac{\partial q}{\partial X_1}\left(\frac{\partial u_1}{\partial X_1}P_{11} + \frac{\partial u_2}{\partial X_1}P_{21} - W\right) + \frac{\partial q}{\partial X_2}\left(\frac{\partial u_1}{\partial X_1}P_{12} + \frac{\partial u_2}{\partial X_1}P_{22}\right)\mathrm{d}S \tag{65}$$

$$J_2(\mathbf{d}) = \int_S \frac{\partial q}{\partial X_1}\left(\frac{\partial u_1}{\partial X_2}P_{11} + \frac{\partial u_2}{\partial X_2}P_{21}\right) + \frac{\partial q}{\partial X_2}\left(\frac{\partial u_1}{\partial X_2}P_{12} + \frac{\partial u_2}{\partial X_2}P_{22} - W\right)\mathrm{d}S. \tag{66}$$

It must be noted that the notation used is the same as [26,27], and our findings reconcile with their results (see Section 5).

Differentiating J with respect to $\mathbf{d}$ requires more effort. Indeed,

$$\frac{\partial J}{\partial \mathbf{d}} = \frac{\partial J_1}{\partial \mathbf{d}}\cos(\theta) + \frac{\partial J_2}{\partial \mathbf{d}}\sin(\theta). \tag{67}$$

Considering that $\mathbf{d} = d_{iI},\ i = 1, 2\ I = 1, \ldots, N$, with N the number of nodes and that

$$u_i = \phi_I d_{iI} \tag{68}$$

then

$$\frac{\partial \mathbf{u}}{\partial \mathbf{X}} = \frac{\partial u_i}{\partial X_j} = \frac{\partial \phi_I}{\partial X_j}d_{iI} \tag{69}$$

hence

$$\frac{\partial}{\partial \mathbf{d}}\frac{\partial \mathbf{u}}{\partial \mathbf{X}} = \frac{\partial}{\partial d_{kI}}\frac{\partial u_i}{\partial X_j} = \frac{\partial \phi_I}{\partial X_j}\frac{\partial d_{iI}}{\partial d_{kI}} = \frac{\partial \phi_I}{\partial X_j}\delta_{ik} \tag{70}$$

$$\frac{\partial W}{\partial \mathbf{d}} = \frac{\partial W}{\partial \mathbf{F}}\frac{\partial \mathbf{F}}{\partial \mathbf{d}} = \mathbf{P}\frac{\partial \mathbf{F}}{\partial \mathbf{d}} = \mathbf{P}\frac{\partial}{\partial \mathbf{d}}\frac{\partial \mathbf{u}}{\partial \mathbf{X}} = P_{ij}\frac{\partial \phi_I}{\partial X_j}\delta_{ik} \tag{71}$$

$$\frac{\partial \mathbf{P}}{\partial \mathbf{d}} = \frac{\partial \mathbf{P}}{\partial \mathbf{F}}\frac{\partial \mathbf{F}}{\partial \mathbf{d}} = \mathcal{A}^{(1)}\frac{\partial}{\partial \mathbf{d}}\frac{\partial \mathbf{u}}{\partial \mathbf{X}} \tag{72}$$

where $\mathcal{A}^{(1)}$ is the *First Elasticity Tensor* (a fourth order tensor). Eq. (72) in index notation is

$$\frac{\partial P_{ij}}{\partial d_{kI}} = \mathcal{A}^{(1)}_{ijkl}\frac{\partial \phi_I}{\partial X_l} \tag{73}$$

$$\begin{aligned}\frac{\partial A_1}{\partial \mathbf{d}} = &\int_S \frac{\partial q}{\partial X_1}\left(\frac{\partial}{\partial \mathbf{d}}\frac{\partial u_1}{\partial X_1}P_{11} + \frac{\partial u_1}{\partial X_1}\frac{\partial P_{11}}{\partial \mathbf{d}} + \frac{\partial}{\partial \mathbf{d}}\frac{\partial u_2}{\partial X_1}P_{21} + \frac{\partial u_2}{\partial X_1}\frac{\partial P_{21}}{\partial \mathbf{d}} - \frac{\partial W}{\partial \mathbf{d}}\right)\\ &+ \frac{\partial q}{\partial X_2}\left(\frac{\partial}{\partial \mathbf{d}}\frac{\partial u_1}{\partial X_1}P_{12} + \frac{\partial u_1}{\partial X_1}\frac{\partial P_{12}}{\partial \mathbf{d}} + \frac{\partial}{\partial \mathbf{d}}\frac{\partial u_2}{\partial X_1}P_{22} + \frac{\partial u_2}{\partial X_1}\frac{\partial P_{22}}{\partial \mathbf{d}}\right)\mathrm{d}S\end{aligned} \tag{74}$$

$$\frac{\partial A_2}{\partial \mathbf{d}} = \int_S \frac{\partial q}{\partial X_1}\left(\frac{\partial}{\partial \mathbf{d}}\frac{\partial u_1}{\partial X_2}P_{11} + \frac{\partial u_1}{\partial X_2}\frac{\partial P_{11}}{\partial \mathbf{d}} + \frac{\partial}{\partial \mathbf{d}}\frac{\partial u_2}{\partial X_2}P_{21} + \frac{\partial u_2}{\partial X_2}\frac{\partial P_{21}}{\partial \mathbf{d}}\right) + \frac{\partial q}{\partial X_2}\left(\frac{\partial}{\partial \mathbf{d}}\frac{\partial u_1}{\partial X_2}P_{12} + \frac{\partial u_1}{\partial X_2}\frac{\partial P_{12}}{\partial \mathbf{d}} + \frac{\partial}{\partial \mathbf{d}}\frac{\partial u_2}{\partial X_2}P_{22} + \frac{\partial u_2}{\partial X_2}\frac{\partial P_{22}}{\partial \mathbf{d}} - \frac{\partial W}{\partial \mathbf{d}}\right) \mathrm{d}S. \tag{75}$$

To facilitate the reproducibility of the results by the reader, the Appendix reports the complete expanded expressions for the derivatives in Eqs. (75) and (74).

4. The *J*-integral based arc-length solver

4.1. The standard arc-length method

A classical arc-length solver seeks the solution $(\mathbf{d}, \lambda)$ for the discretized equation of equilibrium

$$\boldsymbol{\Psi}(\mathbf{d}, \lambda) = \mathbf{F}^{(i)}(\mathbf{d}) - \lambda \mathbf{F}^{(e)} = 0 \tag{76}$$

with $\mathbf{F}^{(i)}(\mathbf{d})$ being the internal force vector, $\mathbf{P}$ is the external force vector and λ is the load level. Eq. (76) is a non-linear system of $2N$ equations in $2N + 1$ unknowns. Hence, it is necessary to add an equation, normally called the spherical *arc-length* constraint

$$g(\mathbf{d}, \lambda) = \Delta\mathbf{d}^T \Delta\mathbf{d} + \psi^2 \Delta\lambda^2 \mathbf{F}^{(e)\,T}\mathbf{F}^{(e)} - l^2 = 0 \tag{77}$$

where l is the arc-length parameter, and $\Delta\mathbf{d} = \mathbf{d} - \mathbf{d}_0$, where $\mathbf{d}_0$ is a previously converged state, ψ is a parameter that is inserted to balance the contributions from both the displacement and the load levels [42]. Fig. 1 depicts the scheme in a simplified one-dimensional example with $\psi \neq 0$ in Eq. (77). With $\psi = 0$, Eq. (77) is known as *cylindrical* arc-length constraint.

In an iterative scheme, the increment $\Delta\mathbf{d}$ towards the next converged state $(\mathbf{d}, \lambda)$ is given by

$$\Delta\mathbf{d}_{k+1} = \Delta\mathbf{d}_k + \delta\mathbf{d}_k \qquad \Delta\lambda_{k+1} = \Delta\lambda_k + \delta\lambda_k \tag{78}$$

where

$$\delta\lambda_k = -\frac{1}{\kappa}(\mathbf{h}^T\mathbf{d}_\psi + g_k) \tag{79}$$

$$\delta\mathbf{d}_k = \mathbf{d}_\psi + \delta\lambda_k \mathbf{d}_e \tag{80}$$

where

$$\kappa = w + \mathbf{h}^T\mathbf{d}_e \tag{81}$$

$$\mathbf{h} = \left(\frac{\partial g}{\partial \mathbf{d}}\right)_k \tag{82}$$

$$w = \left(\frac{\partial g}{\partial \lambda}\right)_k \tag{83}$$

$$g_k = \Delta\mathbf{d}_k^T \Delta\mathbf{d}_k + \psi^2 \Delta\lambda_k^2 \mathbf{F}^{(e)\,T}\mathbf{F}^{(e)} - l^2 \tag{84}$$

$$\mathbf{d_e} = \mathbf{K}_T^{-1}\mathbf{F}^{(e)} \tag{85}$$

where $\mathbf{K}_T$ is the *tangent stiffness matrix*

$$\mathbf{K}_T = \left(\frac{\partial \mathbf{F}^{(i)}}{\partial \mathbf{d}}\right)_k \tag{86}$$

$$\mathbf{d}_\psi = -\mathbf{K}_T^{-1}\boldsymbol{\Psi}_k \tag{87}$$

where

$$\boldsymbol{\Psi}_k = \mathbf{F}^{(i)}(\mathbf{d}_0 + \Delta\mathbf{d}_k) - (\lambda_0 + \Delta\lambda_k)\mathbf{F}^{(e)}. \tag{88}$$

4.2. Dissipation-based arc-length

Gutierrez [15] and Verhoosel et al. [16] proposed an energy release control for failure in brittle and ductile solids. The arc-length constraint is

$$g = \Delta G - \tau \tag{89}$$

where τ is size of the step, and G is the proper *strain energy release rate*, defined as time derivative of energetic quantities

$$G = \dot{P} - \dot{W} \tag{90}$$

where $\dot{P}$ is the *power of the external forces* and $\dot{W}$ the rate of the *strain energy*. It must be remarked that in fracture mechanics, G can also be expressed as a *change in fracture surface area* cf. Eq. (55). Particularly, they presented a scheme for *geometrical* non-linear constitutive models, that is with large displacements and small strains. In these assumptions, Eq. (52) is valid. Instead, in this paper we present a full *large strain–large displacement* model.

To retain the advantageous and clever idea of a dissipation-based arc-length, in this work we propose to compute the strain energy release rate from the J*-integral*, and modify the arc-length constraint to reflect a fracture criterion commonly adopted in fracture mechanics, that is the critical load for crack initiation is such that

$$G = G_c \tag{91}$$

where G_c is the *critical strain energy release rate*, often referred in the literature as *fracture energy*. In addition to the arc-length proposed by Gutierrez [15] and Verhoosel et al. [16], the one proposed in this paper incorporates a criterion for the direction of crack propagation. In addition, the proposed solver operates on actual *rates* (in the fracture mechanics sense) of energy, rather than *increments* of energy.

4.3. The proposed J-integral arc-length constraint

The scheme in Section 4.1 will not necessarily enforce the Griffith energy balance (49) in the presence of a propagating crack, as the numerical example in Section 7.3 demonstrates. Therefore, the constraint in Eq. (77) is replaced by

$$g = J(\mathbf{d}, \theta_{\max}) - G_c \tag{92}$$

where $G = J$ was exploited. In addition, J depends on the orientation of the crack increment. It is reasonable to accept that the crack will propagate in the direction $\theta_{\max}$ of maximum strain energy release rate

$$\theta_{\max} = \arg \max_{\theta \in [0,2\pi]} J(\mathbf{d}, \theta). \tag{93}$$

To summarize, the scheme becomes a *two parameters* arc-length continuation, in θ and λ. For simplicity, only one crack-tip is assumed, but similar arguments can be made for multiple crack tips.

$$\begin{cases} \mathbf{F}^{(i)}(\mathbf{d}) - \lambda \mathbf{F}^{(e)} = \boldsymbol{\Psi}(\mathbf{d}, \lambda) = \mathbf{0} \\ J(\mathbf{d}, \theta_{\max}) - G_c = g(\mathbf{d}, \theta) = 0 \\ \theta - \theta_{\max} = f(\mathbf{d}, \theta) = 0. \end{cases} \tag{94}$$

Hence, in an iterative perspective, the following Newton–Rahpson step is required:

$$\begin{bmatrix} \delta \mathbf{d}_{k+1} \\ \delta \lambda_{k+1} \\ \delta \theta_{k+1} \end{bmatrix} = \begin{bmatrix} \mathbf{K}_T & -\mathbf{F}^{(e)} & 0 \\ \mathbf{h}^T & 0 & \dfrac{\partial J}{\partial \theta} \\ \dfrac{\partial f}{\partial \mathbf{d}}^T & 0 & \dfrac{\partial f}{\partial \theta} \end{bmatrix} \begin{bmatrix} -\boldsymbol{\Psi}_k \\ -g_k \\ -f_k \end{bmatrix}. \tag{95}$$

However, the *two-parameters* continuation in Eq. (94) can be re-formulated as a standard continuation as in Section 4.1. Indeed, Eq. (93) can be solved analytically as later reported in Eq. (102), as it consists in finding the

maximum of function $J(\mathbf{d},\theta)$ as in Eq. (64). It must be remarked that $J(\mathbf{d},\theta)$ can physically only be non-negative, and that it is a continuous periodic function in θ, as $J(\mathbf{d},0) = J(\mathbf{d},2\pi)$. Hence, a local maximum can be easily obtained, as it will be shown in Section 5.

Therefore, assuming that $\theta_{\max}$ is readily obtainable at each iteration, the continuation (94) becomes

$$\begin{cases} \mathbf{F}^{(i)}(\mathbf{d}) - \lambda \mathbf{F}^{(e)} = \boldsymbol{\Psi}(\mathbf{d},\lambda) = \mathbf{0} \\ J(\mathbf{d},\theta_{\max}) - G_c = g(\mathbf{d}) = 0 \end{cases} \tag{96}$$

where $\mathbf{F}^{(e)}$ is defined in Eq. (36) and $\mathbf{F}^{(i)}$ in Eq. (38) and the Newton–Rahpson step

$$\begin{bmatrix} \delta\mathbf{d}_{k+1} \\ \delta\lambda_{k+1} \end{bmatrix} = \begin{bmatrix} \mathbf{K}_T & -\mathbf{F}^{(e)} \\ \mathbf{h}^T & 0 \end{bmatrix} \begin{bmatrix} -\boldsymbol{\Psi}_k \\ -g_k \end{bmatrix} \tag{97}$$

where $\mathbf{h} = \frac{\partial J}{\partial \mathbf{d}}$ is given by Eq. (67).

5. Link with a constitutive theory based on configurational forces [27]

Indeed, with the positions

$$J_1 = |\mathbf{j}|\cos(\beta) \qquad J_2 = |\mathbf{j}|\sin(\beta). \tag{98}$$

Eq. (64) can be arranged as

$$J(\mathbf{d},\theta) = |\mathbf{j}|\left(\cos(\beta)\cos(\theta) + \sin(\beta)\sin(\theta)\right) = |\mathbf{j}|\cos(\beta-\theta). \tag{99}$$

Therefore, the maximum of $J(\mathbf{d},\theta)$ is given by the angle θ satisfying

$$\frac{\partial J}{\partial \theta} = 0 \qquad \frac{\partial^2 J}{\partial \theta^2} < 0 \tag{100}$$

which means

$$\frac{\partial J}{\partial \theta} = -|\mathbf{j}|\sin(\beta-\theta) \qquad \frac{\partial^2 J}{\partial \theta^2} = -|\mathbf{j}|\cos(\beta-\theta)\,. \tag{101}$$

Eqs. (101) are simultaneously satisfied by

$$\theta_{\max} = \beta = \arctan_2(J_2, J_1) \tag{102}$$

which means that the crack propagation direction (for a constitutively isotropic material) $\mathbf{e}$ points in the same direction as the vector $\mathbf{j}$

$$\mathbf{e} = \frac{\mathbf{j}}{|\mathbf{j}|} \tag{103}$$

which is the same result found in [27] (equation 8.11 of their paper). In addition, because of Eq. (99) it is possible to compute *explicitly* the Frank diagram of J.

The Frank diagram of a function $\varphi(\theta)$ describing a curve in polar form $r = \varphi(\theta)$ is defined as

$$\text{Frank}(\varphi) = \left\{ (r,\theta) : r = \frac{1}{\varphi(\theta)} \right\}. \tag{104}$$

Therefore,

$$\text{Frank}(J) = \left\{ (r,\theta) : r = \frac{1}{|\mathbf{j}| cos(\beta-\theta)} \right\} \tag{105}$$

which represents the polar equation of a straight line, as reported in equation 7.18 of [27]. In addition, for *isotropic* crack-tips with *fracture energy* G_c independent of the orientation θ, there is at most *one possible* kinking angle θ, which correspond to $\theta_{\max}$ in Eq. (103). Our finding is then in agreement with this corollary of their *Criticality Theorem*.

6. Strategies for continuation

6.1. Line search

When det $(\mathbf{K}_T)$ is close to zero, the step from Eqs. (79) and (80) can become larger than the radius of convergence of a Newton–Rahpson (NR) scheme. In this case, the residual might increase, while it should, instead, decrease. To recover a descent in the norm of a residual, it is opportune to combine a Newton–Rahpson scheme with a *Line-Search* (LS) algorithm [7]. The idea of a LS is to search for an adequate decrease of the norm of the residual. The problem in Eq. (96) is re-formulated as

$$(\mathbf{d}, \lambda) = \arg\min_{(\mathbf{d},\lambda)} F(\mathbf{d}, \lambda) \qquad F(\mathbf{d}, \lambda) = \frac{1}{2}\boldsymbol{\Psi}(\mathbf{d}, \lambda)^T \boldsymbol{\Psi}(\mathbf{d}, \lambda) + \frac{1}{2} g(\mathbf{d})^2. \tag{106}$$

Since F is a non-negative function in $(\mathbf{d}, \lambda)$, its minimum is also a zero. Hence, Eqs. (106) and (96) have the same solutions.

Instead of taking the full NR step, LS seeks for a fraction η

$$\Delta\mathbf{d}_{k+1} = \Delta\mathbf{d}k + \eta\, \delta\mathbf{d}k \qquad \Delta\lambda_{k+1} = \Delta\lambda_k + \eta\, \delta\lambda_k \tag{107}$$

such that

$$F(\mathbf{d}_{k+1}, \lambda_{k+1}) \leq F(\mathbf{d}_k, \lambda_k) + \eta \left(\frac{\partial F}{\partial \Delta\mathbf{d}}\right)^T \Delta\mathbf{d}_k + \eta \frac{\partial F}{\partial \Delta\lambda}\Delta\lambda_k. \tag{108}$$

The value of η is given by the minimum of the function $f(\eta) = F(\mathbf{d}_k + \eta\Delta\mathbf{d}_k, \lambda_k + \eta\Delta\lambda_k)$. Since the actual function $f(\eta)$ is not known *a priori*, it is assumed quadratic or cubic

$$f(\eta) \approx \left(f(1) - f(0) - \frac{df}{d\eta}(0)\right)\eta^2 + \frac{df}{d\eta}(0)\,\eta + f(0) \tag{109}$$

with

$$\begin{aligned} &f(0) = F(\mathbf{d}_k, \lambda_k) \qquad f(1) = F(\mathbf{d}_{k+1}, \lambda_{k+1}) \\ &\frac{df}{d\eta}(0) = \frac{\partial F}{\partial \Delta\mathbf{d}}\Delta\mathbf{d}_k + \frac{\partial F}{\partial \Delta\lambda}\Delta\lambda_k = \left(\boldsymbol{\Psi}^T\mathbf{K}_T + g\mathbf{h}\right)^T \Delta\mathbf{d}_k + (-\mathbf{F}^{(e)T}\boldsymbol{\Psi})\Delta\lambda_k. \end{aligned} \tag{110}$$

6.2. Pseudo J-integral arc-length for the pre-propagation stage

Fig. 4 shows a typical snap-back in a force–displacement curve occurring for a crack propagating in an elastic solid. The phase OF is the response for an initial crack of length a_0, then at point F the crack starts growing, at which $G = G_c$. All the points in OF are characterized by a value of the strain energy release rate inferior to the critical one. To get to the point F from an initial position 0, one could follow the spherical arc-length (Fig. 4(a)) and then switch to a *J-integral* arc-length. This is because applying the *J-integral* arc-length from point O, would result in getting straight to the point F. It would appear then that the *J-integral* does not capture the intermediate states. In addition, it is sometimes required to proceed through intermediate steps, especially if the displacement at point F is quite large. In fact, this could avoid excessive distortions during each iteration, which could lead to negative Jacobian.

Nonetheless, the proposed arc-length can be easily modified to capture the intermediate states in OF. Indeed, it suffices to replace G_c in Eq. (92) with a value $G_0 < G_c$, and increase it after each converged step until it reaches the critical value G_c. The increment ΔG can be decided, for example, by the number of desired iterations k_d and the number of the actual *corrector* iterations k_c achieved at the previous state. For example, the following law provides a balanced increment in G:

$$G_{0,\text{new}} = \min\left(G_{0,\text{old}} + \Delta G_{\text{new}}, G_c\right) \qquad \Delta G_{\text{new}} = \Delta G_{\text{old}}\left(\frac{k_d}{k_c}\right)^{0.5}. \tag{111}$$

In this paper, we only considered one crack tip, the one with the maximum value of the J-integral. It is possible, in principle, to apply it for each crack-tip and have separate increments of ΔG.

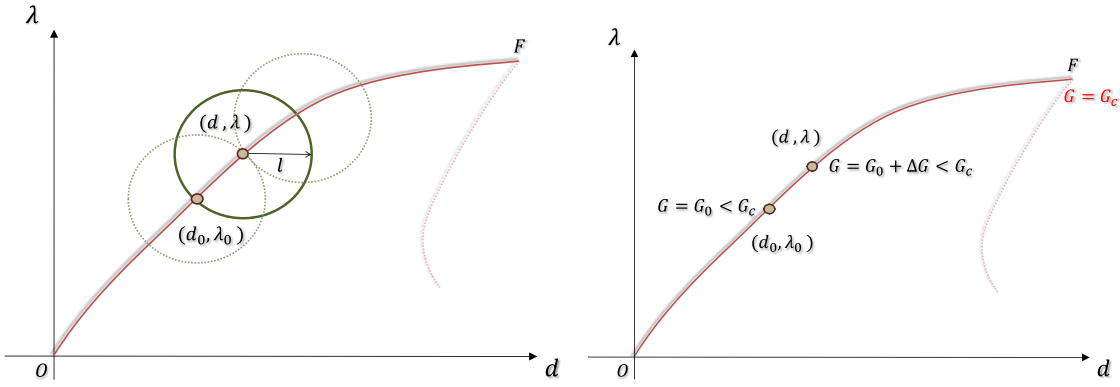

(a) Spherical arc-length. (b) Pseudo J-integral arc-length.

Fig. 4. Pre-propagation stage OF for initial crack length a_0.

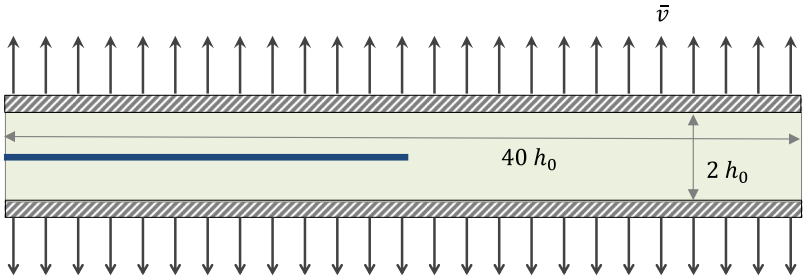

Fig. 5. Tensile test for the *J-integral* solution in Eq. (112): an infinitely long strip of a thin rubber sheet of height $2h_0$, clamped at the top and bottom edges, with an applied displacement $\bar{v}$.

7. Numerical examples

Unless stated otherwise, the examples in this section assume an incompressible Neo-Hookean material model in plane stress (44), with $\mu = 0.4225$ MPa and $G_c = 10\ \mathrm{kJ/m^2}$, values typical of natural rubber.

7.1. Comparison of the J-integral with an analytical solution

Firstly, the accuracy of the numerical J-integral (Eq. (63)) is verified through comparison with an analytical expression [31]. The test is shown in Fig. 5, where, for a Neo-Hookean incompressible solid in plane stress

$$J = \mu\, h_0 \left(\alpha - \frac{1}{\alpha}\right) \tag{112}$$

where the stretch α results from

$$\alpha = 1 + \frac{\bar{v}}{h_0} \tag{113}$$

where $\bar{v}$ is an applied displacement. To mimic an infinitely long strip, the domain of study is rectangular, with height being $2\ h_0$ and length $40\ h_0$, with $h_0 = 0.025$ m. The *mesh size* Δh used is 0.01 m, and the domain $\mathcal{D}_\rho$ for the J-integral had radius $\rho = h_0$. It was seen path-independence for relatively small values of ρ/h. Fig. 6 shows a comparison between computed values of J-integral and Eq. (112). The curves are almost overlapping, with an error of *at most* 1%.

7.2. Verification of the fracture criterion

After having verified the accuracy of the numerical J-integral, we proceed in testing the validity of the assumption at the basis of the fracture criterion in Section 3 and Fig. 3. The idea is recalled and further explained in Fig. 7 for

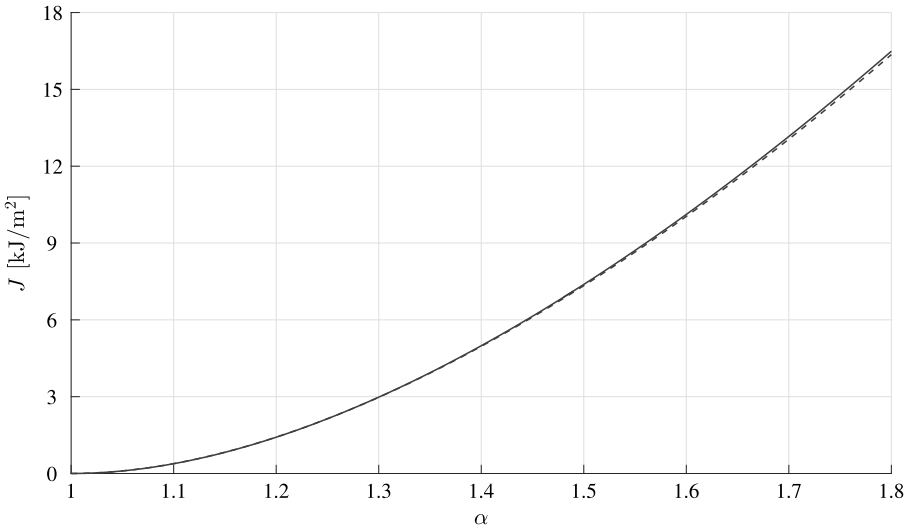

Fig. 6. Validation against the analytical solution in Eq. (112): continuous line: numerical; dashed line: analytical. The error is within 1%.

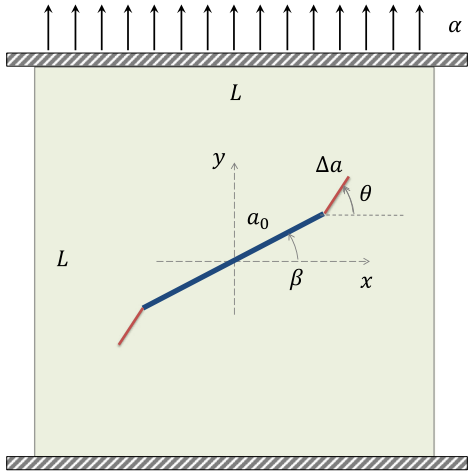

Fig. 7. Verification of the maximum dissipation assumption: a sample with an inclined central crack of length $2a_0$, $a_0 = 0.1\ L$ and initial angle β is stretched (with α being the stretch) uni-axially in displacement control. Given these conditions, two crack kinks (red lines) of inclination θ are added asymmetrically to simulate a crack growth scenario. (For interpretation of the references to colour in this figure legend, the reader is referred to the web version of this article.)

an inclined central crack of a sample stretched uni-axially under displacement control: the value of the J-*integral* at the tip of a kinked crack Δa inclined of θ from an initial crack a_0 inclined of β is the same as the value of the J-integral for the initial crack a_0 *without the kinks*, obtained by simply rotating of θ the relevant fields. Two values of the stretch α are considered, namely $\alpha = 1.2$ and $\alpha = 1.4$, where the stretch α is computed according to Eq. (113). For simplicity, the same value is applied before and after introducing the kinks. Therefore, the value of J after the kinks, will be inevitably higher (Figs. 8(a) and 9(a)). Hence, for a better comparison, the values *after the kinks* are normalized with respect to the maximum value (Figs. 8(b) and 9(b)). For the loading conditions in Fig. 7, it is known that the crack will tend to kink and propagate in a direction orthogonal to the loading ($\theta = 0$). In fact, Figs. 8 and 9 show a maximum at $\theta = 0$, and the shapes of the normalized curves are indeed very similar, with minor discrepancies due to the finiteness of the kinks, whose minimum length is limited by the mesh size Δh. In fact, in principle the kinks Δa should be chosen as small as possible, to be consistent with the *infinitesimal* assumption of the virtual kinks; but, in practice, Δa needs to be sufficiently larger than the value of the radius ρ in $\mathcal{D}_\rho$, which guarantees an accurate and

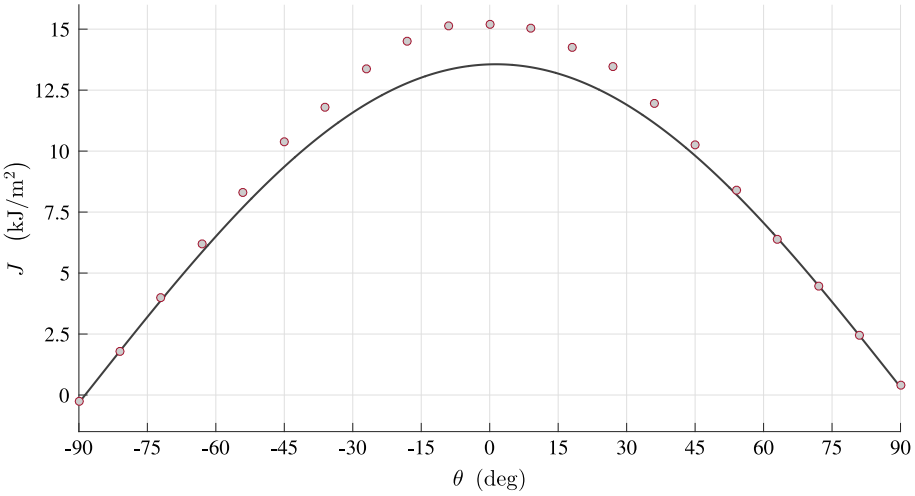

(a) Values of J.

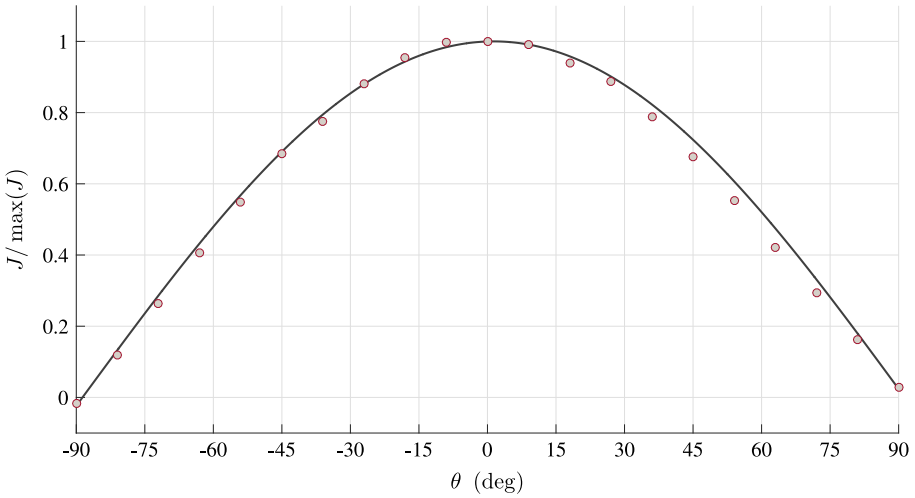

(b) Normalized to the maximum values.

Fig. 8. Variation of J with the inclination θ of the kink for an inclined central crack of $\beta = 30°$ under tensile stretch $\alpha = 1.2$: continuous line, Eq. (64) used at initial crack a_0; dots, numerical values with explicit cracks $a_0 + \Delta a$.

path-independent value of the J-integral. This value of ρ is dictated, in turn, by the mesh size Δh, according to the findings of Section 7.1. In this example, the value of Δh is 5 mm, whilst $\Delta a = 15$ mm.

7.3. Crack propagation with the cylindrical, spherical and proposed arc-length

After having verified the fracture criterion, we proceed next to show that a cylindrical or a spherical arc-length criterion (Eq. (77)) does not necessarily satisfy the onset of the Griffith criterion (Eq. (49)), hence cannot be used in tracing equilibrium curves. The geometry and the boundary conditions are shown in Fig. 10. Fig. 11 shows the equilibrium curves obtained with a cylindrical arc-length (Eq. (77) with $\psi = 0$) and a spherical arc-length (Eq. (77) with $\psi = 1$). The value of the J-integral (Fig. 11(b)) exceeds the critical value G_c. Even if they satisfy the Griffith inequality $G \geq G_c$, they do not provide correct information on the onset of crack propagation for various crack lengths. Instead, Fig. 12(b) illustrates that the value of J remains fixed at G_c for all the subsequent steps. In addition, the equilibrium curve in Fig. 12(a) interestingly shows a *double snap-back* behaviour. The related deformations to critical points 1–4, with the crack openings, are shown in Fig. 13.

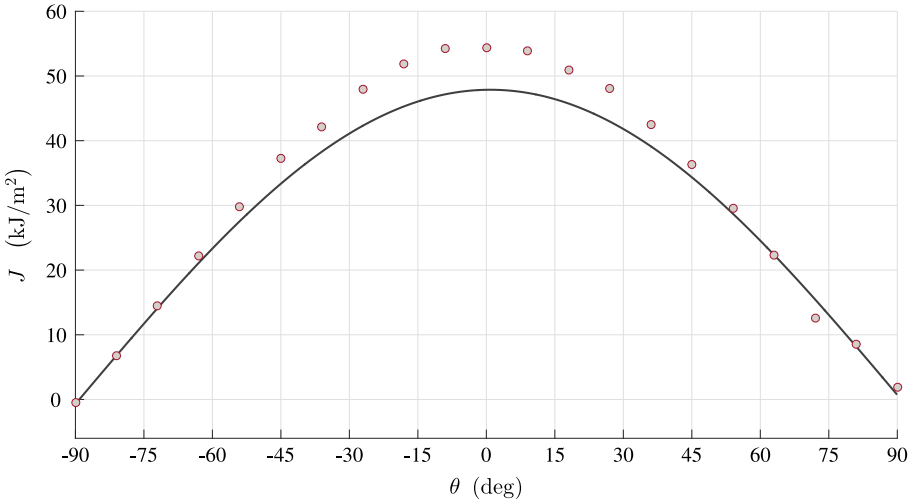

(a) Values of J.

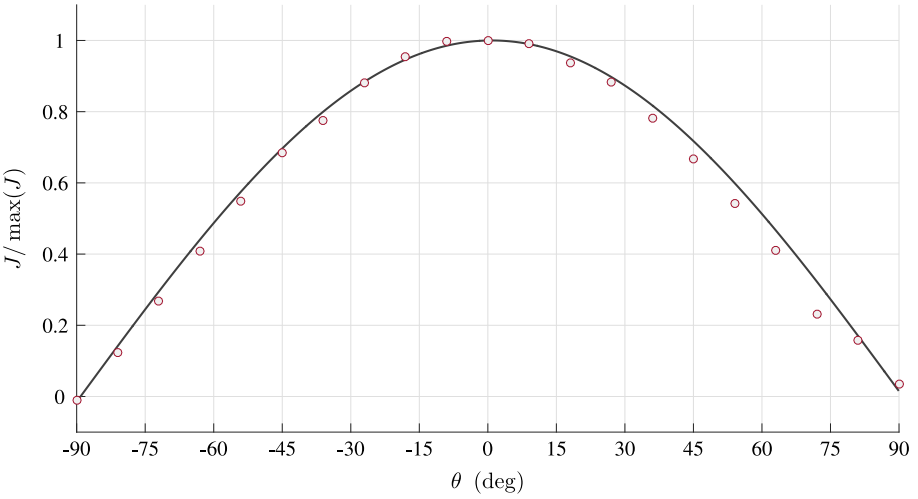

(b) Normalized to the maximum values.

Fig. 9. Variation of J with the inclination θ of the kink for an inclined central crack of $\beta = 30°$ under tensile stretch $\alpha = 1.4$: continuous line, Eq. (64) used at initial crack a_0; dots, numerical values with explicit cracks $a_0 + \Delta a$.

7.4. Double Edge Notched Tensile (DENT)

In this section we consider the crack propagation and interaction of two edge cracks in a specimen under displacement control conditions. In these conditions, the arc-length parameter is the stretch α, and the nominal traction λ is computed as a reaction force. The two cracks are separated by a distance h, symmetrically positioned with respect to the mid-plane of the sample ($y = 0$). Different values of h are considered, including the *collinear* case with $h = 0$. For collinear cracks, both cracks will propagate in a straight direction, until they merge (Fig. 15).

For $h > 0$, the cracks tend to bend anti-symmetrically, to form a lenticular fragment: Fig. 16 shows the equilibrium curve for $h/L = 0.3$ with the relative deformed configurations. The curving of the cracks brings considerable additional stretchability to the structure: for example, with $h/L = 0.3$, the final stretch at complete fracture is higher than the case with $h = 0$, as it can also be seen from the equilibrium curves (Fig. 17).

The *misalignment* length h has a minor effect on the overall strength, but a major non-proportional influence on the *stretch at fracture*. On one hand increasing h can bring the cracks too far apart to intersect (Fig. 18); on the other

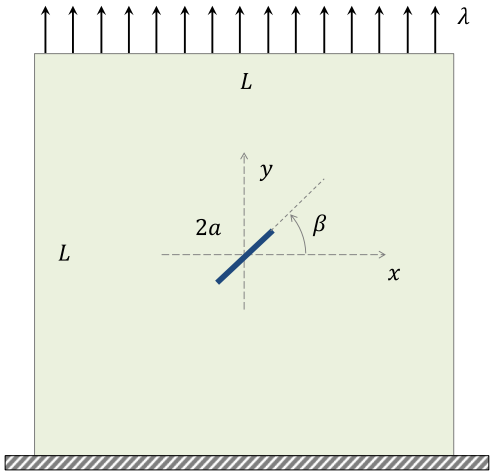

Fig. 10. Numerical example for the cylindrical, spherical and the proposed arc-length method: $L = 1$ m, $a = 0.1\ L$, $\beta = 30°$.

hand, decreasing h can lead the crack path to intersect too soon (for example $h/L = 0.05$) leading to a more *ductile* behaviour, but lower stretch at fracture.

A trend seems to appear, towards an optimal value of h that maximizes the stretch at fracture. For such value, the two cracks intersect in a point that is, at the same time, located on the boundary: for this reason, we will refer to this intersection as a *triple point*.

The value of $h/L = 0.14$ provides this condition, and it seems to be an optimal value for the maximum stretch at fracture (Fig. 19).

Finally, it must be noted that for *relatively high* values of h/L, counter-intuitively, the top crack tends to curve *downwards*. This is a consequence of the large deformations and strains, and it is an effect not predictable by the linear theories. Indeed, for Linear Elastic Fracture Mechanics (LEFM), the path of the crack at the top for $h/L = 0.8$ should have initially curved *upwards*, and then steadily proceed horizontally. This effect is explained more in detail in the next section.

7.5. Comparison with the maximum hoop stress criterion for Linear Elastic Fracture Mechanics (LEFM)

To fit the assumptions of the LEFM, the proposed arc-length method was tested for a ceramic material (Alumina), which exhibits high Young Modulus (corresponding to a shear Modulus $\mu = 165$ GPa), but very low fracture energy $G_c = 60\ \mathrm{J/m^2}$, or, in terms of fracture toughness, $K_c = 5\ \mathrm{MPa}\sqrt{\mathrm{m}}$. The test in Fig. 14 was carried out for $h/L = 0.6$ with two different solvers: (i) the fully non-linear finite deformation with an hyperelastic constitutive model, with the *J-integral-based* arc-length and the fracture criterion proposed in this paper, (ii) a linear elastic solver with a *maximum hoop stress* criterion [43]. The proposed arc-length returns the same results of the maximum hoop stress criterion, in terms of crack paths (Fig. 20) and equilibrium curve (Fig. 21). In addition, Fig. 21 shows that the maximum strain at fracture is around 0.18%, which is consistent with the assumptions of the linear theories.

As anticipated at the end of Section 7.4, the path for the crack at the top predicted by the LEFM, tends to slightly curve upwards, and then propagate orthogonally to the loading direction: instead, for a material with high toughness, the same crack tends to curve *downwards*, as a result of the large deformations.

7.6. Graphene kirigami structures

The previous example shown that it is possible for transition from a brittle to a ductile fracture just by changing the positions of the cracks. Kirigami (from the Japanese *kiru* = to cut, *kami* = paper) is the ancient Japanese art of paper sculptures, and it consists in cutting and stretching a single sheet of paper. The stretch causes the cracks to open, and display the artistic pattern, as shown in Fig. 22. Recently, many authors attempted to design flexible structures following this idea [44–50], and notably [51–53] applied the kirigami idea to graphene materials. The novelty of

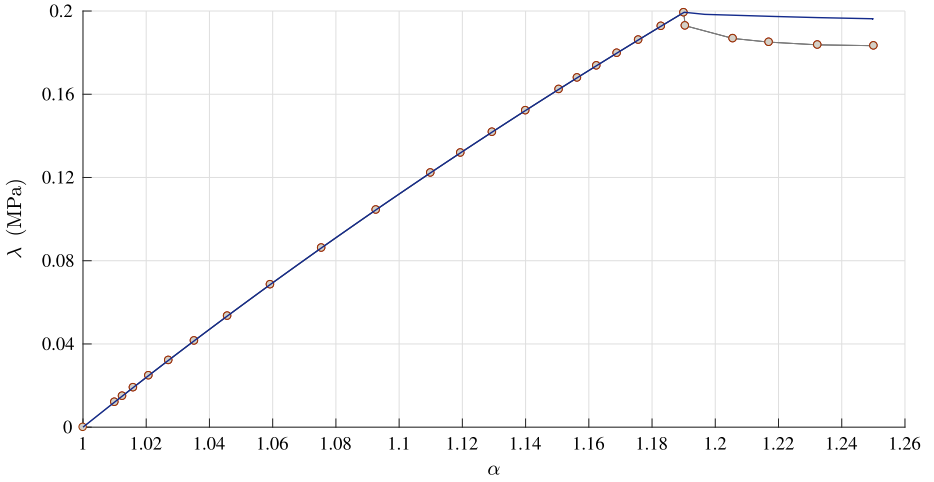

(a) Applied traction level λ as a function of resulting vertical stretch α.

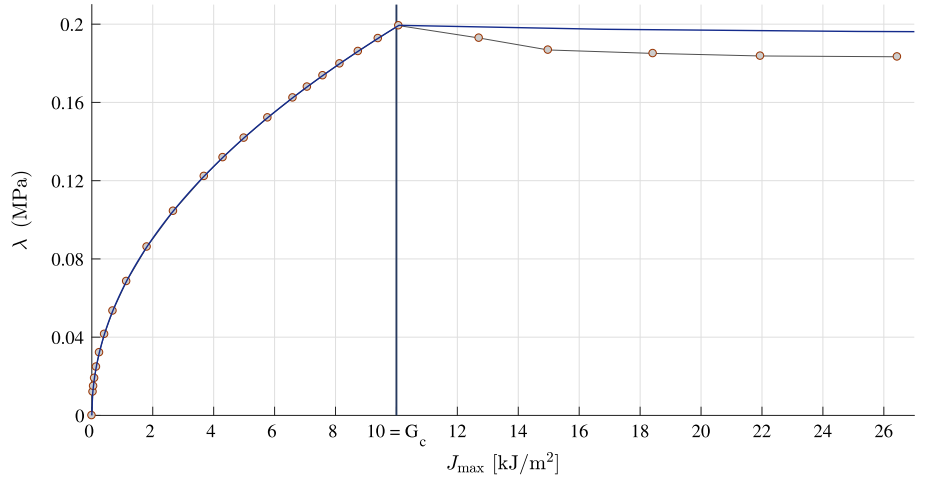

(b) Applied traction level λ as a function of resulting maximum J value.

Fig. 11. Failure of the cylindrical and spherical arc-length in capturing snap back and the correct values of G_c for a growing crack; dotted black line is the cylindrical arc-length, blue thin line is the spherical arc-length with $\psi = 1$. (For interpretation of the references to colour in this figure legend, the reader is referred to the web version of this article.)

this paper is that the proposed arc-length method, combined with the ability of introducing cracks, can predict the maximum stretch at fracture and strength of graphene kirigami sheets. As an example, Fig. 23 depicts a kirigami-style structure, with an alternating pattern of cracks, along the lines of the example in Section 7.4. A sophisticated constitutive model for finite deformation of graphene can be found in [54]: however, for the sake of simplicity, a compressible Neo-Hookean model is used, with energy function

$$W = \frac{1}{2}\mu_0 (I_1 - 3) + \lambda_0 \frac{1}{2} (\log J)^2 - \mu_0 \log J \tag{114}$$

where μ_0 is the *initial* shear modulus, λ_0 the *initial* bulk modulus. For graphene, the following values are used [54]: $E = 1.030$ TPa and $\nu = 0.231$, while the fracture energy $G_c = 15.9\,\mathrm{J/m^2}$ [55]. With reference to Fig. 23, $D = 100$ Å, and $L = 340$ Å. Fig. 24 shows two equilibrium curves for the same type of kirigami structures (same pre-crack patterns): the spacing d between the cuts is the same, but the cuts have different length. It is interesting to see that the structure with shorter cracks has higher strength, but brittle behaviour and lower stretch-at-fracture; instead, the one

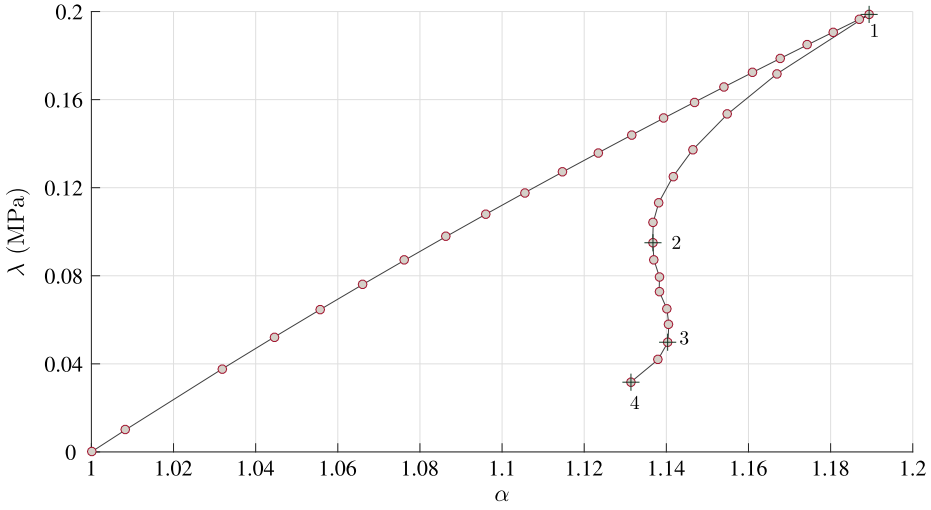

(a) Applied traction level λ as a function of resulting vertical stretch α.

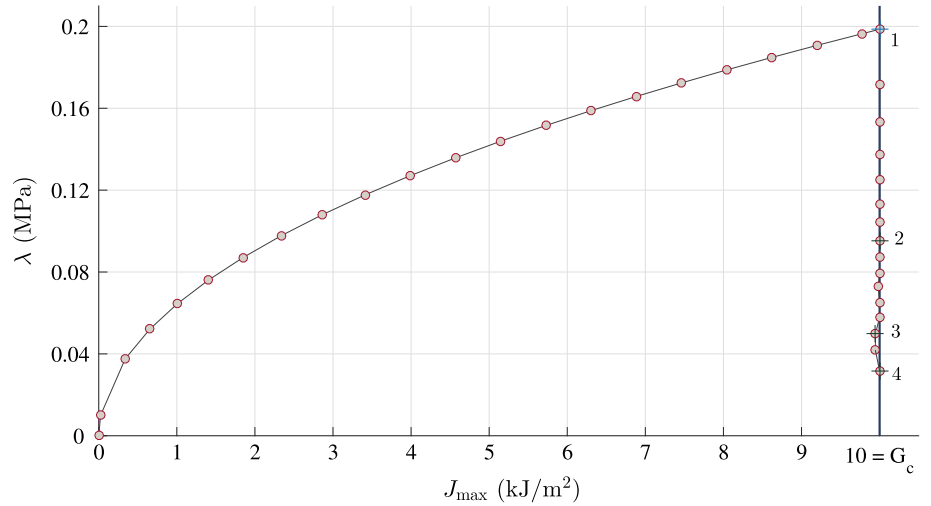

(b) Applied traction level λ as a function of resulting maximum J value.

Fig. 12. *J-integral*-based arc-length: it captures snap back and the correct values of G_c (vertical blue line) for a growing crack. (For interpretation of the references to colour in this figure legend, the reader is referred to the web version of this article.)

with the longer cracks, exhibits a ductile behaviour, with much higher stretch at fracture, albeit with lower strength. Fig. 25 shows all the crack propagation steps for various points on the curve. Ideally, one could use the arc-length in this paper to optimize the design of the cuts such that both high strength and high toughness are achieved.

8. Conclusions

This paper proposed a path-following method for tracing the bifurcation diagram of crack propagation in hyperelastic media, which account for both geometrical and material nonlinearities. Unlike other methods available in the literature, the one presented here does not require the computation of mixed-mode Stress Intensity Factors, and, consequently, the knowledge of asymptotic near crack-tip solutions. This approach incorporates the principle of maximum dissipation rate and thus is thermodynamically consistent. The basis of the proposed method is the rate form of the Griffith balance (Eq. (49)), and requires only the computation of the *J-integral* for rotated stress and displacement gradient fields (Eq. (56)). The assumption behind the method (verified in this paper) is that the fields

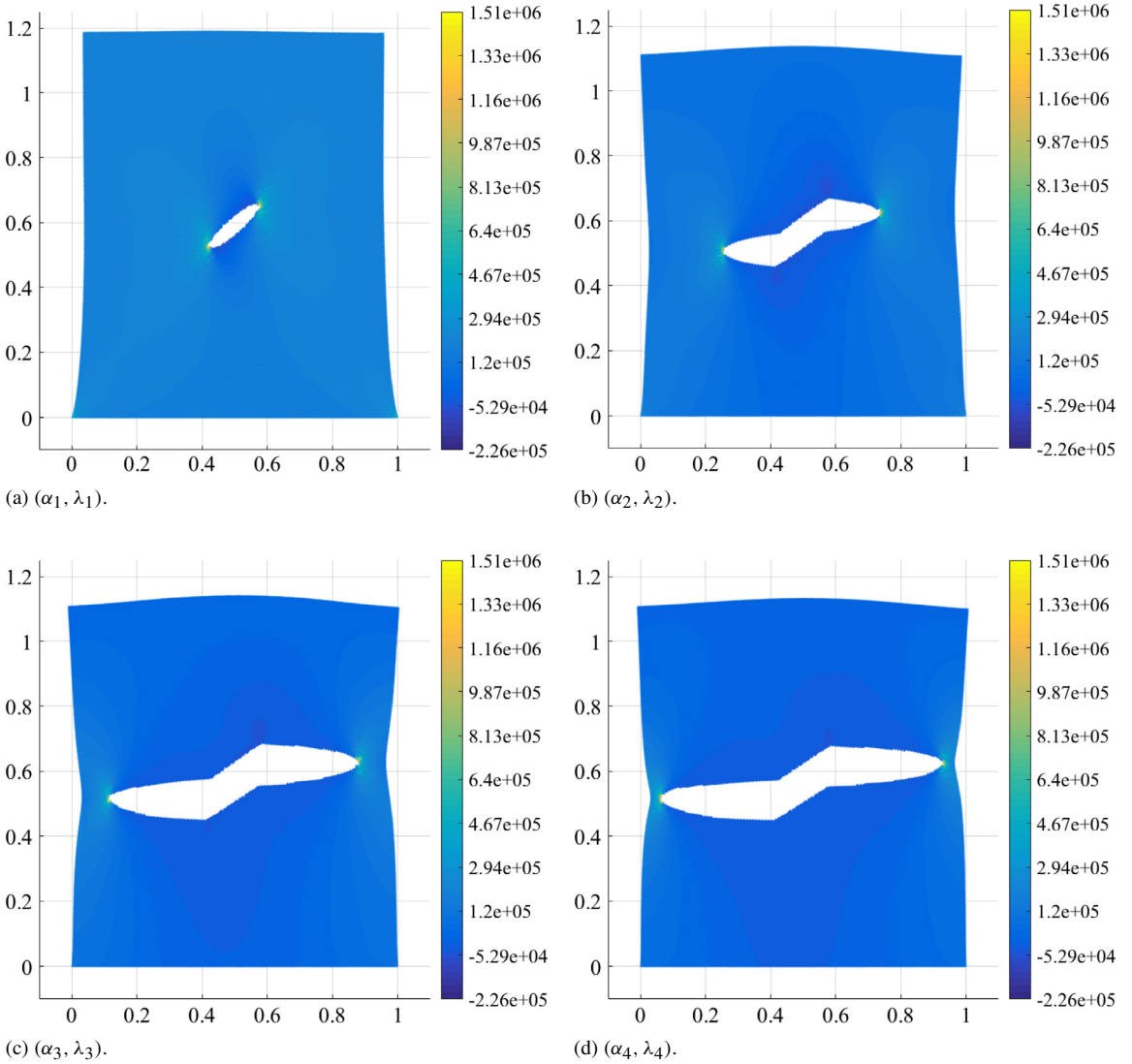

(a) (α_1, λ_1). (b) (α_2, λ_2).

(c) (α_3, λ_3). (d) (α_4, λ_4).

Fig. 13. Deformations of the snap-backs in Fig. 12. Colours show σ_{22} (in Pa). There is a double snap-back: even if the crack is larger at point 3, its maximum vertical displacement is slightly higher than point 2. (For interpretation of the references to colour in this figure legend, the reader is referred to the web version of this article.)

produced by small kinked cracks (Fig. 3) are not substantially different from the ones produced by the initial crack *apart from the related rotation*.

The maximum dissipation assumption leads to an explicit formula for J for varying angles of propagation (Eq. (64)). The maximization of such equation allows to reconcile with a constitutive theory for kinking and curving of cracks based on the theory of Configurational Forces [27].

The results show that the proposed arc-length can handle very sharp snap-back paths in the equilibrium curve (for example, Figs. 12, 17 and 24), and for multiple crack problems. In particular, these examples show that misaligned cracks combined with hyperelastic materials can lead to very deformable structures. The idea of non-collinear cracks can be exploited to design extremely stretchable structures, similar to the Japanese art of paper sculpture (*kirigami*). In combination with the use of high-strength materials, like graphene, it is believed that this could be a pathway to obtain sheets with simultaneous high strength and high toughness.

The examples show the ability of the arc-length solver to predict the large deformations of graphene kirigami sheets, and to capture the transition from brittle to ductile for the same pattern, but with different lengths (Figs. 24 and 25).

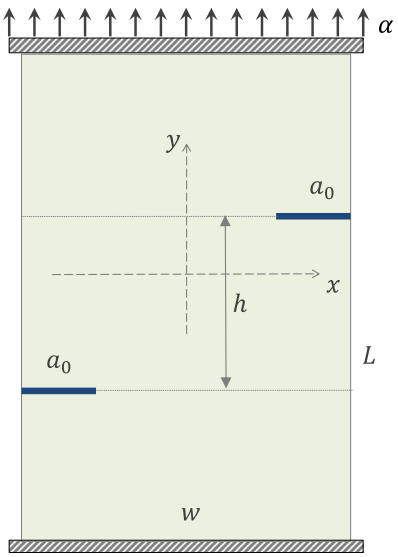

Fig. 14. Double edge cracks tensile tests with applied stretch α: $W = 0.08$ m, $L = 0.2$ m, $a_0 = 16$ mm.

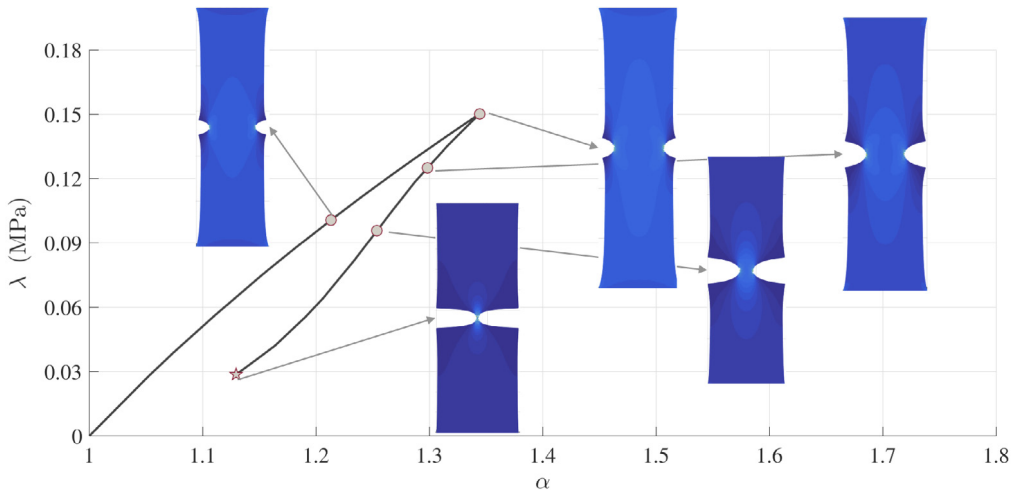

Fig. 15. Double edge collinear cracks tensile tests with applied stretch α: $W = 0.08$ m, $L = 0.2$ m, $a_0 = 16$ mm. Traction-stretch equilibrium curve, along with deformed configurations at dotted points; the star indicates the stretch at complete fracture.

Acknowledgments

EB and FO are supported by the Queen Mary University of London Start-up grant for new academics. N.M.P. is supported by the European Research Council (ERC StG Ideas 2011 BIHSNAM No. 279985, ERC PoC 2015 SILKENE No. 693670), and by the European Commission under the Graphene Flagship (WP14 Polymer Nanocomposites, No. 696656). The authors would like to thank the artist Mizuho Ozaki for the kirigami sculptures.

Appendix. Full expressions of the consistent linearization of the J-integral

In the following,

$$\boldsymbol{\phi}^T = \begin{bmatrix} \phi_1(\mathbf{X}) & \phi_2(\mathbf{X}) & \dots & \phi_N(\mathbf{X}) \end{bmatrix} \quad I = 1, \dots, N \tag{A.1}$$

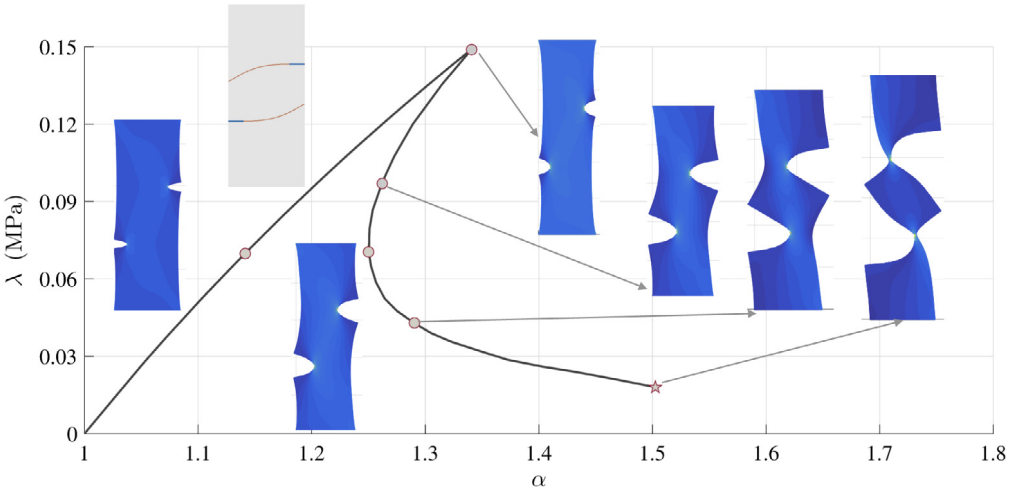

Fig. 16. Double edge non-collinear cracks tensile tests with applied stretch α: $W = 0.08$ m, $L = 0.2$ m, $h = 0.06$ m, $h/L = 0.3$, $a_0 = 16$ mm. Traction-stretch equilibrium curve, along with deformed configurations at dotted points; crack paths on the undeformed configuration are shown on the left. The star indicates the stretch at complete fracture.

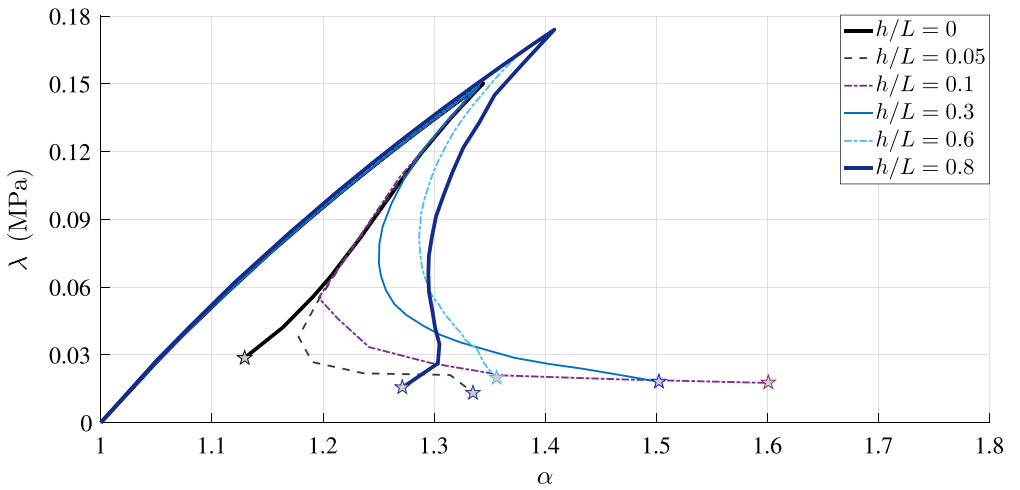

Fig. 17. Double edge non-collinear cracks tensile tests: comparison of equilibrium curves for increasing h/L. The star at the end of each curve indicates the stretch at complete fracture.

$$\frac{\partial}{\partial \mathbf{d}}\frac{\partial u_1}{\partial X_1} = \begin{bmatrix} \dfrac{\partial \boldsymbol{\phi}}{\partial X_1} \\ 0 \end{bmatrix} \tag{A.2}$$

$$\frac{\partial}{\partial \mathbf{d}}\frac{\partial u_1}{\partial X_2} = \begin{bmatrix} \dfrac{\partial \boldsymbol{\phi}}{\partial X_2} \\ 0 \end{bmatrix} \tag{A.3}$$

$$\frac{\partial}{\partial \mathbf{d}}\frac{\partial u_2}{\partial X_1} = \begin{bmatrix} 0 \\ \dfrac{\partial \boldsymbol{\phi}}{\partial X_1} \end{bmatrix} \tag{A.4}$$

$$\frac{\partial}{\partial \mathbf{d}}\frac{\partial u_2}{\partial X_2} = \begin{bmatrix} 0 \\ \dfrac{\partial \boldsymbol{\phi}}{\partial X_2} \end{bmatrix} \tag{A.5}$$

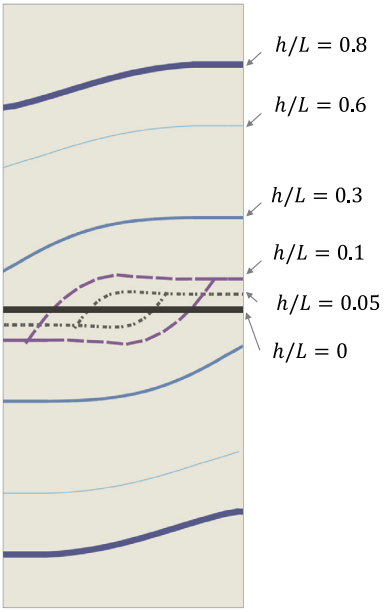

Fig. 18. Double edge non-collinear cracks tensile tests: comparison of crack paths in the *reference configuration* for varying h.

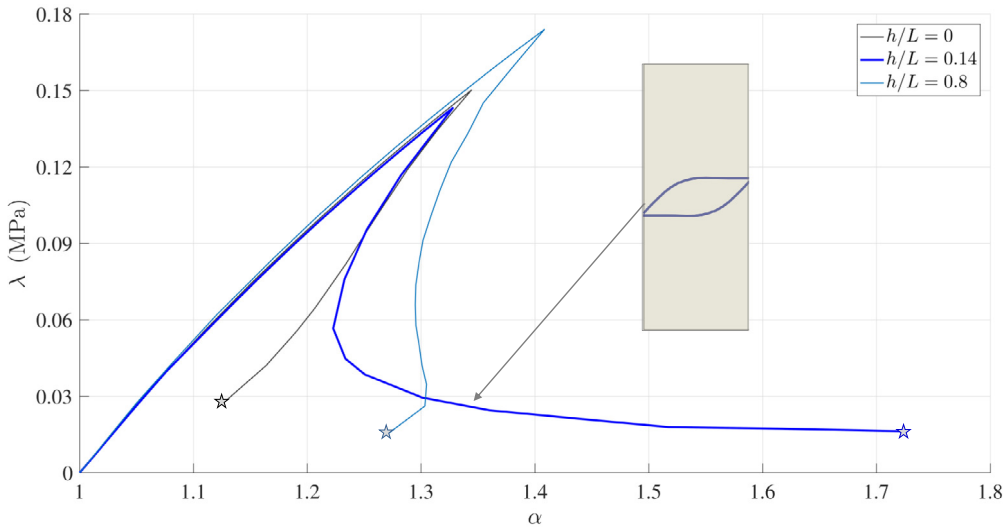

Fig. 19. Double edge non-collinear cracks tensile tests: optimal h/L for maximum stretch at fracture. The value of $h/L = 0.14$ causes the crack paths to join at a *triple point*. The star at the end of each curve indicates the stretch at complete fracture.

$$\frac{\partial W}{\partial \mathbf{d}} = \begin{bmatrix} P_{11}\dfrac{\partial \boldsymbol{\phi}}{\partial X_1} + P_{12}\dfrac{\partial \boldsymbol{\phi}}{\partial X_2} \\ P_{21}\dfrac{\partial \boldsymbol{\phi}}{\partial X_1} + P_{22}\dfrac{\partial \boldsymbol{\phi}}{\partial X_2} \end{bmatrix} \tag{A.6}$$

$$\frac{\partial P_{11}}{\partial \mathbf{d}} = \begin{bmatrix} \mathcal{A}^{(1)}_{1111}\dfrac{\partial \boldsymbol{\phi}}{\partial X_1} + \mathcal{A}^{(1)}_{1112}\dfrac{\partial \boldsymbol{\phi}}{\partial X_2} \\ \mathcal{A}^{(1)}_{1121}\dfrac{\partial \boldsymbol{\phi}}{\partial X_1} + \mathcal{A}^{(1)}_{1122}\dfrac{\partial \boldsymbol{\phi}}{\partial X_2} \end{bmatrix} \tag{A.7}$$

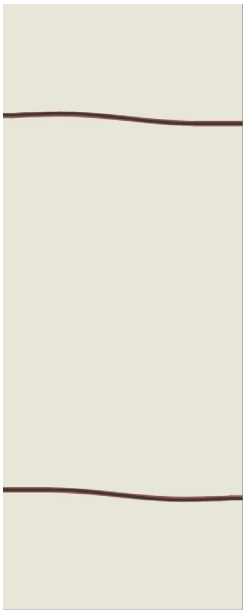

Fig. 20. Double edge non-collinear cracks tensile tests for alumina and for $h/L = 0.6$: comparison of crack paths between the proposed arc-length (red line) and the *maximum hoop stress criterion* (black line). (For interpretation of the references to colour in this figure legend, the reader is referred to the web version of this article.)

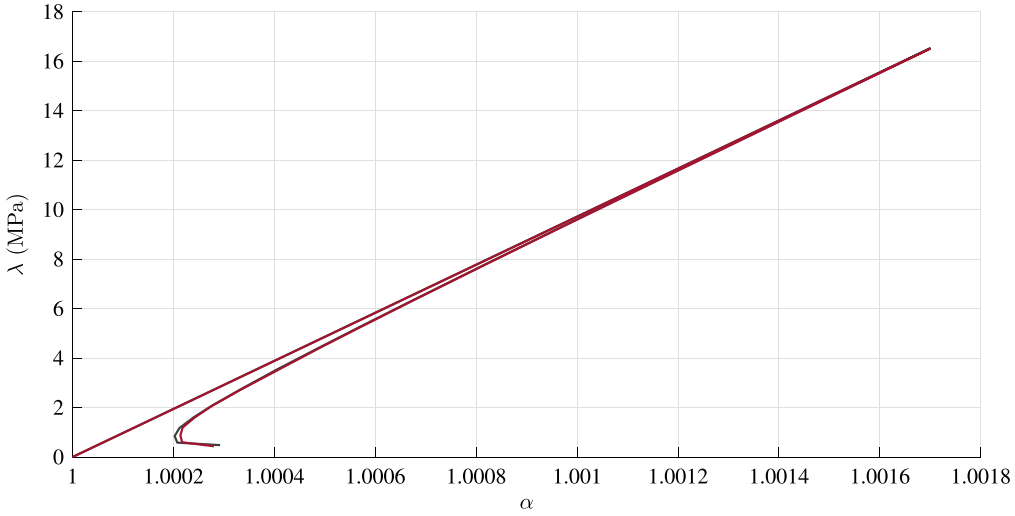

Fig. 21. Double edge non-collinear cracks tensile tests for alumina and for $h/L = 0.6$: comparison of equilibrium curves between the proposed arc-length (red line) and the *maximum hoop stress criterion* (black line). (For interpretation of the references to colour in this figure legend, the reader is referred to the web version of this article.)

$$\frac{\partial P_{12}}{\partial \mathbf{d}} = \begin{bmatrix} \mathcal{A}^{(1)}_{1211} \dfrac{\partial \boldsymbol{\phi}}{\partial X_1} + \mathcal{A}^{(1)}_{1212} \dfrac{\partial \boldsymbol{\phi}}{\partial X_2} \\ \mathcal{A}^{(1)}_{1221} \dfrac{\partial \boldsymbol{\phi}}{\partial X_1} + \mathcal{A}^{(1)}_{1222} \dfrac{\partial \boldsymbol{\phi}}{\partial X_2} \end{bmatrix} \tag{A.8}$$

$$\frac{\partial P_{21}}{\partial \mathbf{d}} = \begin{bmatrix} \mathcal{A}^{(1)}_{2111} \dfrac{\partial \boldsymbol{\phi}}{\partial X_1} + \mathcal{A}^{(1)}_{2112} \dfrac{\partial \boldsymbol{\phi}}{\partial X_2} \\ \mathcal{A}^{(1)}_{2121} \dfrac{\partial \boldsymbol{\phi}}{\partial X_1} + \mathcal{A}^{(1)}_{2122} \dfrac{\partial \boldsymbol{\phi}}{\partial X_2} \end{bmatrix} \tag{A.9}$$

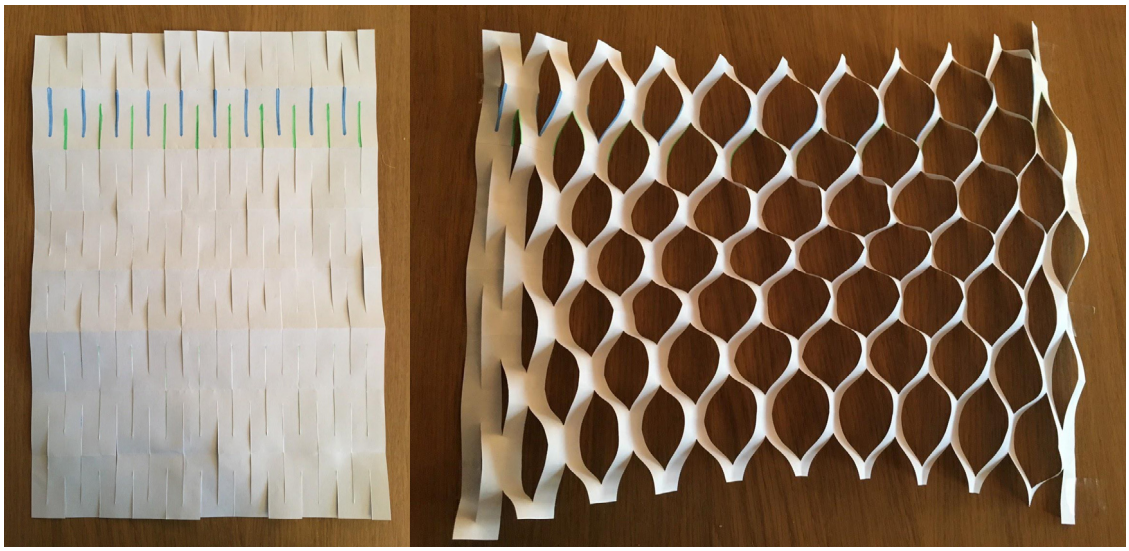

Fig. 22. Example of kirigami paper sculpture. The photo on the left shows the cutting pattern, with blue and green highlights evidencing the staggered configuration.The photo on the right shows the artistic pattern after stretching the sheet with a uniaxial horizontal force. Photo courtesy of artist Mizuho Ozaki.

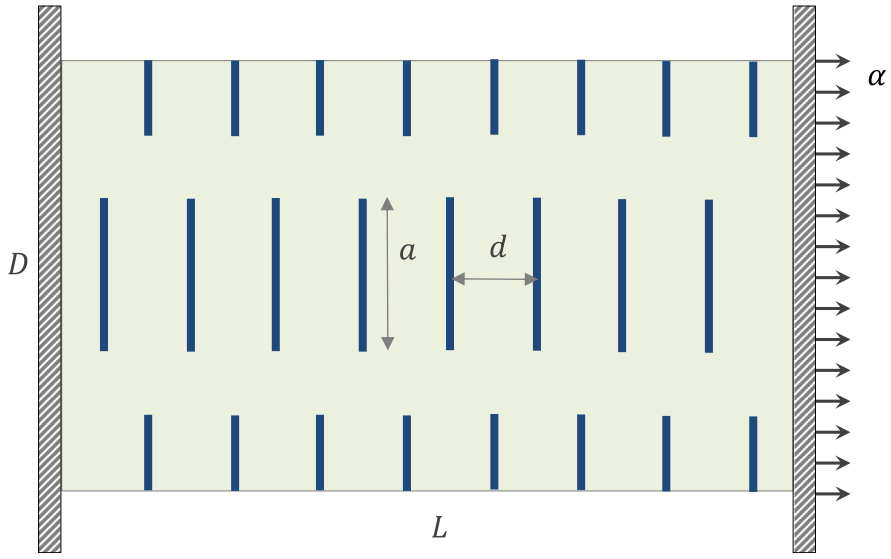

Fig. 23. Tensile test in displacement control of a graphene kirigami structure.

$$\frac{\partial P_{22}}{\partial \mathbf{d}} = \begin{bmatrix} \mathcal{A}^{(1)}_{2211}\dfrac{\partial \boldsymbol{\phi}}{\partial X_1} + \mathcal{A}^{(1)}_{2212}\dfrac{\partial \boldsymbol{\phi}}{\partial X_2} \\ \mathcal{A}^{(1)}_{2221}\dfrac{\partial \boldsymbol{\phi}}{\partial X_1} + \mathcal{A}^{(1)}_{2222}\dfrac{\partial \boldsymbol{\phi}}{\partial X_2} \end{bmatrix}. \tag{A.10}$$

The *First Elasticity Tensor* $\mathcal{A}^{(1)}$ can be obtained by the *Second Elasticity Tensor* $\mathcal{A}^{(2)}$ from

$$\mathcal{A}^{(1)}_{ijkl} = \delta_{ik}\delta_{jl} + F_{in}\mathcal{A}^{(2)}_{njml}F_{km} \tag{A.11}$$

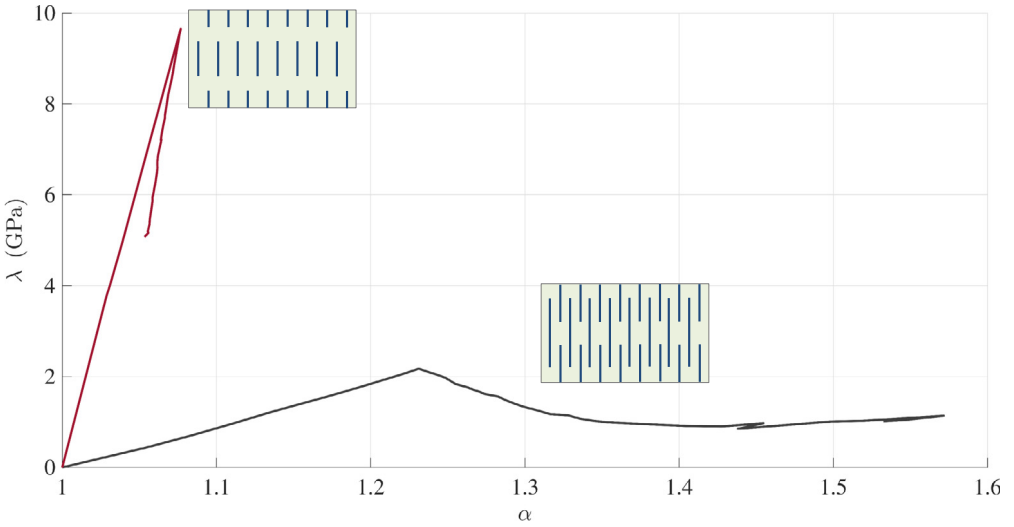

Fig. 24. Equilibrium curve for a tensile test in displacement control of a graphene kirigami structure: red line $d = 36$ Å, $a = 41$ Å; black line $d = 36$ Å, $a = 76$ Å. (For interpretation of the references to colour in this figure legend, the reader is referred to the web version of this article.)

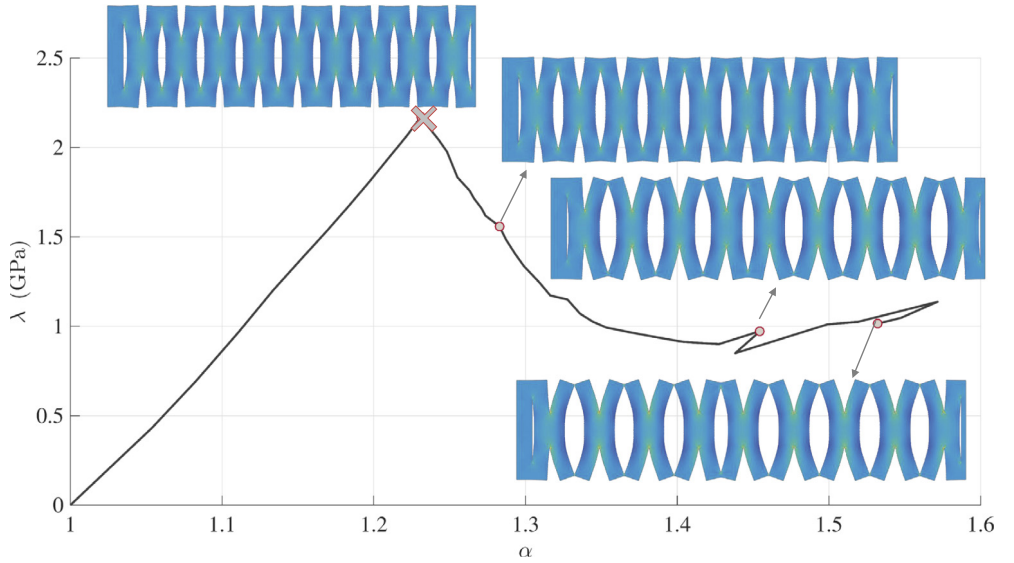

Fig. 25. Graphene kirigami structure with $d = 36$ Å, $a = 41$ Å (Fig. 23): traction–stretch equilibrium curve, along with deformed configurations at points. Beyond the critical fracture initiation point (indicated by the cross), the crack pattern is *stable*, such that it allows further stretching. The same pattern, but with shorter cracks, instead propagates in an unstable manner (red line of Fig. 24).

where F_{ij} is the deformation gradient

$$\mathcal{A}^{(2)} = 4\frac{\partial^2 W}{\partial \mathbf{C}\partial \mathbf{C}} = 2\frac{\partial \mathbf{S}}{\partial \mathbf{C}}. \tag{A.12}$$

References

[1] J.P. Abbott, Numerical continuation methods for nonlinear equations and bifurcation problems, Bull. Aust. Math. Soc. 17 (02) (1977) 307–308.
[2] E.L. Allgower, K. Georg, Numerical continuation methods, in: Springer Series in Computational Mathematics, vol. 13, Springer-Verlag, Berlin, 1990.
[3] E.L. Allgower, K. Georg, Introduction to Numerical Continuation Methods, vol. 45, SIAM, 2003.

[4] W. Lacarbonara, Nonlinear Structural Mechanics: Theory, Dynamical Phenomena and Modeling, Springer Science & Business Media, 2013.
[5] E. Riks, The application of Newton's method to the problem of elastic stability, J. Appl. Mech. 39 (4) (1972) 1060–1065.
[6] E. Riks, An incremental approach to the solution of snapping and buckling problems, Int. J. Solids Struct. 15 (7) (1979) 529–551.
[7] M. Crisfield, An arc-length method including line searches and accelerations, Internat. J. Numer. Methods Engrg. 19 (9) (1983) 1269–1289.
[8] G. Alfano, M. Crisfield, Solution strategies for the delamination analysis based on a combination of local-control arc-length and line searches, Internat. J. Numer. Methods Engrg. 58 (7) (2003) 999–1048.
[9] R. De Borst, Computation of post-bifurcation and post-failure behavior of strain-softening solids, Comput. Struct. 25 (2) (1987) 211–224.
[10] I. May, Y. Duan, A local arc-length procedure for strain softening, Comput. Struct. 64 (1) (1997) 297–303.
[11] B.W. Forde, S.F. Stiemer, Improved arc length orthogonality methods for nonlinear finite element analysis, Comput. Struct. 27 (5) (1987) 625–630.
[12] B. Cochelin, N. Damil, M. Potier-Ferry, Asymptotic–numerical methods and Pade approximants for non-linear elastic structures, Internat. J. Numer. Methods Engrg. 37 (7) (1994) 1187–1213.
[13] A. Elhage-Hussein, M. Potier-Ferry, N. Damil, A numerical continuation method based on Padé approximants, Int. J. Solids Struct. 37 (46) (2000) 6981–7001.
[14] A. Hamdaoui, B. Braikat, N. Damil, Solving elastoplasticity problems by the asymptotic numerical method: Influence of the parameterizations, Finite Elem. Anal. Des. 115 (2016) 33–42.
[15] M.A. Gutierrez, Energy release control for numerical simulations of failure in quasi-brittle solids, Commun. Numer. Methods Eng. 20 (1) (2004) 19–29.
[16] C.V. Verhoosel, J.J. Remmers, M.A. Gutiérrez, A dissipation-based arc-length method for robust simulation of brittle and ductile failure, Internat. J. Numer. Methods Engrg. 77 (9) (2009) 1290–1321.
[17] N. Singh, C.V. Verhoosel, R. de Borst, E.H. van Brummelen, A fracture-controlled path-following technique for phase-field modeling of brittle fracture, Finite Elem. Anal. Des. 113 (2016) 14–29.
[18] S. May, J. Vignollet, R. de Borst, A new arc-length control method based on the rates of the internal and the dissipated energy, Eng. Comput. 33 (1) (2016) 100–115.
[19] K.S. Lee, S.E. Han, T. Park, A simple explicit arc-length method using the dynamic relaxation method with kinetic damping, Comput. Struct. 89 (1) (2011) 216–233.
[20] D.A. Aruliah, L. Van Veen, A. Dubitski, Algorithm 956: PAMPAC, A parallel adaptive method for pseudo-arclength continuation, ACM Trans. Math. Software 42 (1) (2016).
[21] C. Kuehn, Efficient gluing of numerical continuation and a multiple solution method for elliptic PDEs, Appl. Math. Comput. 266 (2015) 656–674.
[22] M. Hintermueller, J. Rasch, Several path-following methods for a class of gradient constrained variational inequalities, Comput. Math. Appl. 69 (10) (2015) 1045–1067.
[23] H. Uecker, D. Wetzel, J.D.M. Rademacher, pde2path-A Mat lab package for continuation and bifurcation in 2D elliptic systems, Numer. Math. Theory Methods Appl. 7 (1) (2014) 58–106.
[24] A.A. Griffith, The phenomena of rupture and flow in solids, Philos. Trans. R. Soc. Lond. Ser. A Math. Phys. Eng. Sci. (1921) 163–198.
[25] G.A. Maugin, Material forces: concepts and applications, Appl. Mech. Rev. 48 (5) (1995) 213–245.
[26] M.E. Gurtin, P. Podio-Guidugli, Configurational forces and the basic laws for crack propagation, J. Mech. Phys. Solids 44 (6) (1996) 905–927.
[27] M.E. Gurtin, P. Podio-Guidugli, Configurational forces and a constitutive theory for crack propagation that allows for kinking and curving, J. Mech. Phys. Solids 46 (8) (1998) 1343–1378.
[28] P. Steinmann, Application of material forces to hyperelastostatic fracture mechanics. I. Continuum mechanical setting, Int. J. Solids Struct. 37 (48) (2000) 7371–7391.
[29] P. Steinmann, D. Ackermann, F. Barth, Application of material forces to hyperelastostatic fracture mechanics. II. Computational setting, Int. J. Solids Struct. 38 (32) (2001) 5509–5526.
[30] P. Podio-Guidugli, Configurational forces: are they needed? Mech. Res. Commun. 29 (6) (2002) 513–519.
[31] A. Thomas, Rupture of rubber. II. The strain concentration at an incision, J. Polym. Sci. 18 (88) (1955) 177–188.
[32] A. Thomas, Rupture of rubber. V. Cut growth in natural rubber vulcanizates, J. Polym. Sci. 31 (123) (1958) 467–480.
[33] A. Thomas, Rupture of rubber. VI. Further experiments on the tear criterion, J. Appl. Polym. Sci. 3 (8) (1960) 168–174.
[34] W. Liu, S. Jun, Y. Zhang, Reproducing kernel particle methods, Internat. J. Numer. Methods Fluids 20 (8–9) (1995) 1081–1106.
[35] E. Barbieri, N. Petrinic, M. Meo, V. Tagarielli, A new weight-function enrichment in meshless methods for multiple cracks in linear elasticity, Internat. J. Numer. Methods Engrg. 90 (2) (2012) 177–195.
[36] E. Barbieri, N. Petrinic, Three-dimensional crack propagation with distance-based discontinuous kernels in meshfree methods, Comput. Mech. (2013) 1–18.
[37] E. Barbieri, N. Petrinic, Multiple crack growth and coalescence in meshfree methods with a distance function-based enriched kernel, in: Key Engineering Materials—Advances in Crack Growth Modeling, TransTech Publications, 2013, p. 170.
[38] E. Barbieri, M. Meo, A fast object-oriented Matlab implementation of the reproducing kernel particle method, Comput. Mech. 49 (5) (2012) 581–602.
[39] R. Sevilla, E. Barbieri, NURBS distance fields for extremely curved cracks, Comput. Mech. 54 (6) (2014) 1431–1446.
[40] T. Belytschko, W.K. Liu, B. Moran, Nonlinear Finite Elements for Continua and Structures, John Wiley & Sons, 2000.
[41] G. Legrain, N. Moes, E. Verron, Stress analysis around crack tips in finite strain problems using the extended finite element method, Internat. J. Numer. Methods Engrg. 63 (2) (2005) 290–314.
[42] R. De Borst, M.A. Crisfield, J.J. Remmers, C.V. Verhoosel, Nonlinear Finite Element Analysis of Solids and Structures, John Wiley & Sons, 2012.
[43] F. Erdogan, G. Sih, On the crack extension in plates under plane loading and transverse shear, J. Basic Eng. 85 (4) (1963) 519–525.

[44] Y. Chen, F. Scarpa, C. Remillat, I. Farrow, Y. Liu, J. Leng, Curved kirigami SILICOMB cellular structures with zero Poisson's ratio for large deformations and morphing, J. Intell. Mater. Syst. Struct. (2013) 1045389X13502852.
[45] R. Neville, A. Monti, K. Hazra, F. Scarpa, C. Remillat, I. Farrow, Transverse stiffness and strength of kirigami zero-ν peek honeycombs, Compos. Struct. 114 (2014) 30–40.
[46] T.C. Shyu, P.F. Damasceno, P.M. Dodd, A. Lamoureux, L. Xu, M. Shlian, M. Shtein, S.C. Glotzer, N.A. Kotov, A kirigami approach to engineering elasticity in nanocomposites through patterned defects, Nat. Mater. (2015).
[47] S. Yang, I.-S. Choi, R.D. Kamien, Design of super-conformable, foldable materials via fractal cuts and lattice kirigami, MRS Bull. 41 (02) (2016) 130–138.
[48] Y. Zhang, Z. Yan, K. Nan, D. Xiao, Y. Liu, H. Luan, H. Fu, X. Wang, Q. Yang, J. Wang, et al., A mechanically driven form of kirigami as a route to 3D mesostructures in micro/nanomembranes, Proc. Natl. Acad. Sci. 112 (38) (2015) 11757–11764.
[49] P.Z. Hanakata, Z. Qi, D.K. Campbell, H.S. Park, Highly stretchable MoS 2 kirigami, Nanoscale 8 (1) (2016) 458–463.
[50] R.M. Neville, F. Scarpa, A. Pirrera, Shape morphing kirigami mechanical metamaterials, Sci. Rep. 6 (2016) 31067.
[51] Z. Qi, D.K. Campbell, H.S. Park, Atomistic simulations of tension-induced large deformation and stretchability in graphene kirigami, Phys. Rev. B 90 (24) (2014) 245437.
[52] M.K. Blees, A.W. Barnard, P.A. Rose, S.P. Roberts, K.L. McGill, P.Y. Huang, A.R. Ruyack, J.W. Kevek, B. Kobrin, D.A. Muller, et al., Graphene kirigami, Nature (2015).
[53] B.F. Grosso, E. Mele, Bending rules in graphene kirigami, Phys. Rev. Lett. 115 (19) (2015) 195501.
[54] M. Xu, J.T. Paci, J. Oswald, T. Belytschko, A constitutive equation for graphene based on density functional theory, Int. J. Solids Struct. 49 (18) (2012) 2582–2589.
[55] P. Zhang, L. Ma, F. Fan, Z. Zeng, C. Peng, P.E. Loya, Z. Liu, Y. Gong, J. Zhang, X. Zhang, et al., Fracture toughness of graphene, Nat. Commun. 5 (2014).